



3 1293 01104 1815

LIBRARY
Michigan State
University

This is to certify that the

thesis entitled

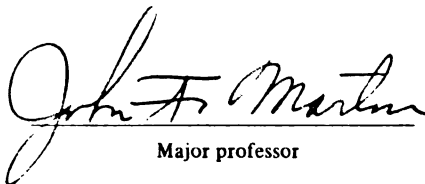
Elevated-Temperature Fretting and Oxidation
Processes of Nickel-Base Superalloy
Turbine Blade Attachments

presented by

Kim K. van den Ende

has been accepted towards fulfillment
of the requirements for

M.S. degree in Materials Science
Engineering


Major professor

Date 11/13/87



RETURNING MATERIALS:
Place in book drop to
remove this checkout from
your record. FINES will
be charged if book is
returned after the date
stamped below.

MAGIC 2

JAN 11 1999

**ELEVATED-TEMPERATURE FRETTING AND OXIDATION PROCESSES
OF NICKEL-BASE SUPERALLOY TURBINE BLADE ATTACHMENTS**

By

Kim K. van den Ende

A THESIS

**Submitted to
Michigan State University
in partial fulfillment of the requirements
for the degree of**

MASTER OF SCIENCE

Department of Metallurgy, Mechanics and Materials Science

1987

ABSTRACT

ELEVATED-TEMPERATURE FRETTING AND OXIDATION PROCESSES OF NICKEL-BASE SUPERALLOY TURBINE BLADE ATTACHMENTS

By

Kim K. van den Ende

Fir-tree turbine blade attachment specimens of Mar-M 247 DS, a directionally solidified Ni-base superalloy, were fatigue tested in air to failure at 650°C. With a new replication technique, Reprosil/Spurr's resin, negative replicas were periodically produced throughout the fatigue lives. Positive resin replicas were analyzed with scanning electron microscopy to study surface reactions in the attachment areas during the simulated service conditions. Microstructures and fracture characteristics were examined to help correlate surface phenomena with the fatigue failure mechanisms.

Two surface-changing features were identified on the fir-tree attachment replicas which influenced the fatigue failures. 1. Extensive fretting wear occurred on the contact regions, with spherical fretting debris and oxide "glaze" development. 2. Brittle "polyp" phases containing micro-cracks developed and were found to be the product of preferential oxidation of carbides. The resulting failure of the specimens was due to fretting fatigue with the fatigue cracks initiating from the oxide polyps and propagating from near the fretted slip/no-slip boundary.

ACKNOWLEDGMENTS

This thesis project was funded by a grant from Garrett Turbine Engine Company of Phoenix, Arizona.

I would like to thank Major Joesph Marksteiner, Patti Lang, Mark Waterbury, Bob Dreshfield, Henry deGroh and Hendrik van den Ende for their help with this project. I would also like to thank my mother for her continued support and love. Finally I would like to give special thanks to Dr. John Martin for his advise, guidance and support.

TABLE OF CONTENTS

	Page
List of Figures	vii
List of Tables	xiii
Chapter 1. Introduction	1
Chapter 2. Literature Review	4
2.1 Physical Metallurgy of Ni-Base Superalloys	4
2.1.1 Matrix (γ)	5
2.1.2 Gamma Prime (γ')	5
2.1.3 Carbides	5
2.1.4 Other Phases (TCP, Borides)	8
2.2 Strengthening Mechanisms of Ni-Base Superalloys .	9
2.2.1 Solid-Solution Strengthening	9
2.2.2 Precipitation Strengthening	10
2.3 Deformation of Ni-Base Superalloys	12
2.4 Microstructural Instabilities	15
2.5 Oxidation of Ni-Base Superalloys	17
2.6 Directional Solidification	22
2.7 Fretting	27
2.8 Fatigue	31
2.9 Fretting Fatigue	33
2.10 Replication	36
Chapter 3. Materials and Experimental Procedures	39
3.1 Materials	39

TABLE OF CONTENTS (Continued)

	Page
3.2 Specimen Geometries	43
3.3 Experimental Procedures	47
3.3.1 Fatigue Testing	47
3.3.2 Load Train	47
3.3.3 Fir-Tree Replicas	48
3.4 Microstructural Examination	50
Chapter 4. Results and Discussion	52
4.1 Fatigue Data	52
4.2 Microstructural Analysis	57
4.2.1 Dendritic Structure	57
4.2.2 Carbides	59
4.2.3 Gamma Prime (γ')	66
4.3 Fir Tree Replicas	66
4.3.1 Fretting Wear	69
4.3.2 Preferential Oxidation	76
4.3.3 Fatigue Cracks	79
4.4 Macroscopic Examination	81
4.4.1 Fretting Wear	81
4.4.2 Fractography	84
4.5 Microscopic Examination	89
4.5.1 Fractography	89
4.5.2 Crack Nucleation	92
4.6 Incipient Melting	101
Chapter 5. Conclusions	109

TABLE OF CONTENTS (Continued)

	Page
Appendix A: Metallography Preparation	113
Appendix B: TEM Replicas	114
B.1 Materials	114
B.2 Procedures	115
Appendix C: Fir-tree Replicas: Procedures and Evaluation	117
C.1 Materials	117
C.2 Procedures	118
C.2.1 Preparation for Making Positive Replicas ...	118
C.2.2 Preparation for Making Negative Replicas ...	119
C.2.3 Making Negative Replicas	120
C.2.4 Making Positive Replicas	122
C.2.5 Preparation for SEM Examination	123
C.3 Evaluation of the Replication Technique	124
List of References	138

LIST OF FIGURES

Figure	Page
1. Schematic illustration of the creation of anti-phase boundary (APB) bonds (a) formed by a dislocation moving through an ordered precipitate, and APB annihilation by a trailing dislocation (9).	13
2. Schematic diagram illustrating the sequence of steps that take place during the development of NiO (Group I), Cr ₂ O ₃ (Group II) and Al ₂ O ₃ (Group III) scales on Ni-Cr-Al alloys. The amount of transient oxides formed prior to the development of a continuous layer of a given oxide depends upon the alloy composition (19).	19
3. Proposed solidification sequence illustrating segregation associated with solidification (26). ...	24
4. Schematic illustration of the formation of columnar grains having [100] orientation. Each columnar grain is oriented randomly about the vertical axis (9).	25
5. Principle of directional solidification (27).	25
6. Stage I and Stage II modes of transgranular fatigue crack growth (54).	34
7. Systems diagram illustrating numerous factors in fretting fatigue (37).	34
8. The F109 jet turbine engine.	40
9. Fir-tree attachment specimen and loading fixtures. 0.4 X	41
10. Specimen specifications, crowned geometries (61). ..	44
11. Loading fixture specifications (61).	45
12. Turbine blade asymmetry (61).	46
13. Complete load train (61).	49
14. Specimen F109-4 Cr, A end, loading grip #5. 3.8X ..	53

LIST OF FIGURES (Continued)

Figure	Page
15. Specimen F109-10 Cr, A end, loading grip #3. 1.55X .	53
16. Loading grip #4 containing a crack initiating from a load bearing surface. 5.5X	54
17. Illustration of nomenclature used for describing specific locations on the fir-tree specimens and for the corresponding loading grip areas.	56
18. Directionally solidified dendritic structure sectioned longitudinal to columnar grains. OM 50X .	58
19. Directionally solidified dendritic structure sectioned transverse to columnar grains. OM 50X ...	58
20. Serrated dendritic, or grain boundaries. OM 200X ..	60
21. Grain boundary carbides. OM 400X	60
22. Microstructure showing large eutectic pools (dark), carbide particles (white) and dendritic areas of fine γ/γ' (grey). SEM 307X	61
23. Blocky MC-type carbide. SEM 3,970X	61
24. Chinese-script (rosette) MC-type carbides. OM 400X .	62
25. Small discrete $M_{23}C_6$ -type carbides. SEM 467X	62
26. Analytical electron microscopy (AEM) dot patterns of script-type carbides, a. back scattered electrons, b. carbon, c. hafnium, d. tantalum, e. titanium, f. molybdenum and g. tungsten. AEM 400X	63
27. A micropore associated with a carbide. SEM 2,470X .	67
28. Cubic morphology and aligned directionality of gamma prime precipitates. RTEM 19,000X	67
29. Gamma prime coarsening. RTEM 29,000X	68
30. Carbide particle surrounded by a continuous layer of gamma prime (dark), and randomly coarsened gamma prime precipitates. SEM 9,980X	68

LIST OF FIGURES (Continued)

Figure	Page
31. Different stages of fretting wear formed in contact regions. Specimen F109-14 Cr, RSEM 150X; a. initial rough adhesive wear (7,441 cycles), b. smoothing down of the initial damage (15K cycles), c. development of spherical fretting particles (25K cycles), note sphere formation is in region of excessive wear in a., d. retention of spherical particle and continued flattening of rougened area with associated "glaze" formation (30K cycles) and e. parallel abrasive grooves in glazed area and surface damage at fretting sphere location (N ₁ =32K).	72
32. Excessive surface damage caused by a spherical fretting debris particle. SEM 500X	74
33. Three fretting spheres located in fretted region. RSEM 38X	74
34. Spherical fretting debris; a. localized roughening, 15K cycles, b. sphere formation at roughened areas. RSEM 100X	75
35. Development of oxide polyps. Specimen F109-1 F; a. 0 cycles, b. 1587 cycles, c. 16,641 cycles, d. 31,587 cycles and e. 46,587 cycles. RSEM 300X ..	77
36. Oxide polyps with inherent cracks. SEM 1000X	80
37. Oxide polyps with a script-morphology. RSEM 300X ..	80
38. Crack of specimen F109-10 Cr; a. no evident of crack at 8,228 cycles and b. crack following dense path of polyps at 14,444 cycles. RSEM 190X	82
39. Crack of Specimen F109-1 F developed between cycles 31,587 and 46,587, this crack runs near the fretted slip/no-slip boundary and also extends into the notched region. RSEM 150X, 300X	83
40. Macrograph of a localized gouged area within a shiny and grooved glazed fretted region.....	86
41. Side view of a "typical" fracture, the directionally solidified dendritic structure is visible. OM 6X ..	86
42. Fracture surface of the longest life specimen, F109-1 F, showing an extensive Stage I region (bright) in a thumbnail crack propagation region. OM 5X	88

LIST OF FIGURES (Continued)

Figure	Page
43. Fracture surface of the shortest life specimen, F109-3, displaying a shorter Stage I region. OM 4X .	88
44. Micrograph of the extensive Stage I region of specimen F109-1 (extending approximately 15mm). SEM 30X	90
45. The smoothness or planarity of Stage I crack propagation is seen in this micrograph where two planes of crack growth intersect. SEM 500X	90
46. Intersecting slip steps in Stage I crack growth region. SEM 500X	91
47. Intersecting slip steps on the order of 10 microns in Stage I crack growth region. SEM 1000X	91
48. Final fracture region characterized by a rough almost dimple-like surface and secondary cracking. SEM 380X	93
49. A faceted, planar fracture region (middle right) with perpendicularly intersecting lines in rough overload, non-planar region. SEM 150X	93
50. Faceted fracture region with intersecting perpendicular lines in final fracture region. SEM 380X ...	94
51. Carbides with script-type morphologies illustrating perpendicularly intersecting lines and other shapes found on faceted fractured surfaces. OM 200X	94
52. The smooth Stage I mode of crack propagation is abruptly changed at a script carbide. The drawing distinguishes the carbide particles which have been darkened. SEM 250X	95
53. Propagation of the fracture crack from the slip/no-slip fretted boundary. SEM 50X	97
54. Initiation site of a fatigue crack at an oxide polyp. SEM 750X	97
55. A deep oxide polyp area caused the plane of fracture to separate. SEM 300X	98
56. Nucleation of a fatigue crack from an oxide polyp. SEM 750X	99

LIST OF FIGURES (Continued)

Figure	Page
57. Nucleation of a fatigue crack from an oxide polyp near the slip/no-slip fretted boundary (upper section of picture). SEM 1000X	99
58. A group of oxide polyyps initiating fatigue cracks near the fretted boundary, note the wear region extending over the crack in the upper right corner. SEM 500X	100
59. Opening up of a fracture region at an oxide polyp at the fretted slip/no-slip boundary (right side). The brittleness of the polyp is illustrated by the secondary cracking. SEM 380X	100
60. Replicas of specimen F109-10 Cr showing the introduction of splashed spheres; a. 0 cycles, b. 1,500 cycles, c. 8,228 cycles and d. 14,444 cycles. RSEM 150X	102
61. Incipient melting splashed sphere on F109-5 F, similar to those in figure 60. SEM 1000X	104
62. Dripping sphere: incipient melting area characterized by glassy, very smooth appearance. SEM 500X ..	104
63. Evidence of incipient melting (feature in lower left area). Cracking at oxide polyyps. SEM 375X ...	105
64. A spherical particle located just inside the boundary of the wear region where localized melting has occurred and recorded the cyclic movement in the smooth melted region. SEM 1500X	105
65. Replica of large surface discontinuity on specimen F109-14 Cr having characteristics of melting and rapidly solidifying; melt droplets, melt craters and solidification shrinkage cracks. RSEM 50X	107
66. Higher magnification of Figure 65 showing quenched droplets from splashing of molten metal and rapid solidification cracks. RSEM 750X	107
67. Splashed quenched droplets radiating away from the large surface discontinuity in Figure 65. SEM 150X .	108
68. Large surface discontinuity on Specimen F109-1 F. SEM 150X	108

LIST OF FIGURES (Continued)

Figure	Page
69. Fir-tree specimen, supported by large paper clip, centered in quartz constraining container. Note adequate air space surrounds specimen to allow for a uniform, thick layer of Reprosil. 0.8X	125
70. A thin streak-free, bubble-free, layer of Reprosil catalyst and base (50/50) is applied to the specimen surface. The container is then filled and the specimen set inside.	125
71. After the Reprosil is hardened, the quartz container is disassembled for easy, non-damaging removal of both the specimen and the replica together.	126
72. Replica steps, from left to right; a. the Reprosil negative replica is cut in half and trimmed, b. the two halves are "glued" together and a ridge is made around the top edge with additional Reprosil, c. the Spurr's resin is poured and cured in the negative replica mold (the positive permanent replica), and d. the positive resin replica is coated with gold. .	126
73. Replica of a fretting sphere near the fretted boundary of specimen F109-1 F taken at 31,587 cycles. RSEM 75X	128
74. Replication of spherical and protruding features: a. replica at 46,587 cycles, 1000X, b. specimen with N ₁ =51,309. 1900X	129
75. Direct comparison of replica and corresponding specimen area: a. specimen 500X (25KV) and b. replica 500X (15KV).	130
76. Replica quality comparison: a. replica 1000X (15KV) and b. specimen 1250X (25KV).	131
77. Replica loses some detail at higher magnification: a. specimen 2500X (25KV) and b. replica 2500X (15KV). It should be noted that a relatively thick coat of gold was applied to these replicas and they are examined at lower accelerating voltages.	132
78. Replicating sequence of specimen F109-4 Cr: a. 0 cycles, b. 1,500 cycles, c. 15,000 cycles, d. 25,000 cycles and e. 35,000 cycles. RSEM 300X ..	135

LIST OF TABLES

Table	Page
1. Nominal Chemical Compositions (Wt. %)	47
2. Specimen Fatigue Results	55
3. Resin Components	118

CHAPTER 1

INTRODUCTION

The demand for increased fuel efficiency of jet turbine engines has been achieved through the development of improved materials which allow for increased operating temperatures. This increase in service temperature is paralleled with increases in mechanical stresses, thermal cycling and environmental attack. One such material advancement is the development of columnar grain (CG) and single-crystal (SC) turbine blades through directional solidification (DS). Polycrystalline directionally solidified blades have longitudinal columnar grain structures with grain boundaries parallel to the major stress axis, and with essentially no grain boundaries normal to the main load. Grain boundaries are sources for sliding, void formation and crack initiation during deformation. Directionally solidified materials are highly anisotropic and display superior fatigue and creep resistant properties compared with conventionally cast materials. Directionally solidified single-crystal blades contain no grain boundaries and have the best over all properties.

--

A major problem associated with directionally solidified

turbine blades, similar to those of conventionally cast alloys, is the fracture of the blade in the attachment area. When the failure is in the blade attachment area the entire blade breaks off and causes serious engine damage. Turbine engine damage, which has been caused by attachment fractures, has made it necessary to investigate the physical metallurgy and mechanical properties of attachment areas. Although this area of research is new, one approach to the problem is to produce attachment specimens and employ a replication technique to record physical changes occurring during simulated service test conditions.

The common replication technique used in materials science research involves cellulose acetate replicating tape, which is small (1 inch wide), brittle, and tends to warp when the technique is applied to curved or notched surfaces. These features can have very undesirable consequences when replicating surfaces such as those of attachment areas. To overcome these problems a new two-stage replication technique, employing Reprosil dental impression medium and Spurr's low-viscosity resin, has been examined and evaluated in its ability to replicate large curved surfaces.

To investigate failures in attachment areas, fir-tree attachment specimens and loading grips were produced. The specimens were fatigue tested in air at 650°C. The objectives of this research were to produce replicas of the fir-tree areas periodically throughout the fatigue lives. Then with the

replicas, study the surface reactions occurring in the attachment areas during the simulated service conditions, and to correlate the surface phenomena with the fatigue failure mechanisms.

CHAPTER 2

LITERATURE REVIEW

The following literature review covers several topics pertinent to this research project. Subjects such as Ni-base superalloys, directional solidification, fatigue, fretting and replication are covered for the benefit of those who might not have background knowledge on these fields.

2.1 PHYSICAL METALLURGY OF NICKEL-BASE SUPERALLOYS

The physical metallurgy of nickel-base superalloys is complex, subtle, and sophisticated. These alloys exhibit outstanding high-temperature mechanical strength and corrosion resistance. Nickel-base alloys have been used in service temperatures up to $0.9T_m$ (1), where T_m is the absolute melting temperature of the alloy. The high-temperature strength properties which make these materials "super" alloys are associated with the unusual behavior of maintaining a constant (or increasing) flow stress with increasing temperature, up to approximately 1400°F. The phases and effects of alloying elements are summarized below.

2.1.1. Matrix (Gamma)

The continuous matrix is an FCC nickel-base austenitic phase, which contains a high percentage of solid solution elements such as cobalt, chromium, molybdenum, and tungsten (2).

2.1.2 Gamma Prime (γ')

The intermetallic phase gamma prime (γ') is an ordered precipitate which binds coherently to the matrix. Gamma prime has the approximate chemical composition $\text{Ni}_3(\text{Al,Ti})$ and has an L1_2 structure with nickel atoms occupying the face centers and aluminum and titanium atoms occupying the cube corners. The nickel can be substituted to some extent by chromium, cobalt, molybdenum or vanadium and the aluminum and titanium can be substituted by niobium, molybdenum, chromium, vanadium and tungsten depending upon alloy composition (3). Single phase γ' remains ordered up to its melting point (4).

2.1.3 Carbides

The role of carbides in superalloys is complex and dynamic (5). Detrimental and beneficial effects have been associated with carbides, but in general carbides are incorporated to increase the stress-rupture properties at elevated temperatures by preventing grain boundary sliding. The most common classes of carbides found in nickel-base superalloys include MC, M_{23}C_6 ,

and M_6C types.

MC-type carbides usually have a coarse random cubic or a chinese-script (rosette) morphology. They are believed to form shortly below freezing as discrete particles distributed both intergranularly and transgranularly (6), and are often found interdendritically. These primary carbides are FCC in structure, very strong and very stable. There is a preferred order of formation for these carbides which has been found empirically to be HfC, TaC, NbC, TiC and VC, in order of decreasing stability (5). Less reactive elements such as Mo and W can also be found in these carbides. Script-type MC carbides in the grain boundaries are known to deteriorate the tensile ductility because they provide crack initiation sites as well as crack propagation paths (7).

Carbides of the $M_{23}C_6$ -types usually occur as irregular discontinuous blocky particles along grain boundaries. These $M_{23}C_6$ carbides have complex cubic structures. Continuous and/or denuded grain boundary $M_{23}C_6$ carbides can adversely affect ductility and rupture life (5). These carbides form during lower-temperature heat treatment and service (1400-1800 °F, 760-980 °C), both from degeneration of MC carbides and from soluble carbon residual in the alloy matrix (5). In contrast the discontinuous $M_{23}C_6$ -type carbides located at grain boundaries are found to have a significant beneficial effect on rupture-strength, as the discrete particles "pin" grain

boundaries and prevent elevated-temperature grain boundary sliding (8). Eventually, however, these carbides are also responsible for the initiation of rupture failures through either their fracture or by decohesion of the $M_{23}C_6$ /matrix (gamma) interface (5). Cellular structures of $M_{23}C_6$ are deleterious phases but can be avoided by proper chemistry and heat treatment control.

M_6C -type carbides can precipitate in blocky form at grain boundaries, and rarely in deleterious Widmanstätten intergranular morphology at higher temperatures (1500-1800°F, 814-980°C). They have complex cubic structures and usually form where refractory metal content is high. Typical formulas include $(Ni,Co)_3Mo_3C$ and $(Ni,Co)_2W_4C$, but a range of formulas from M_3C to $M_{13}C$ have been associated with the M_6C -type carbides (5). M_6C is more stable at higher temperatures than $M_{23}C_6$.

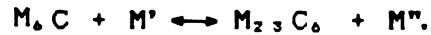
During heat treatment and service, MC carbides can decompose initiating several important reactions. The dominating carbide reaction is believed to be the creation of $M_{23}C_6$ and is represented by the following reaction:



Similarly M_6C can form:



M_6C and $M_{23}C_6$ can also interact:



These reactions are based on strong empirical evidence (5). Most beneficial is the reaction yielding $M_{23}C_6$ carbides at grain boundaries. As mentioned previously, these carbides inhibit grain boundary sliding and the γ' generated through this reaction surrounds the carbides and the grain boundaries in a relatively ductile creep-resistant layer (5). It should also be noted that $M_{23}C_6$ contain large amounts of chromium, hence the surroundings become Cr-depleted during the development of these carbides, giving rise to initiation points of stress-corrosion cracking (7).

Because of the reactions stated above, the distribution and morphology of $M_{23}C_6$ and M_6C depend largely on the primary MC formed. Thus the control of the morphology and distribution of MC carbides is important for the development of superior mechanical properties.

2.1.4 Other Phases (TCP, Borides)

Borides of the M_3B_2 -type usually form in Ni-base superalloys. This type of boride is hard and the morphology varies from blocky to half-moon shaped. Borides supply boron to the

grain-boundary, where it reduces the onset of grain boundary tearing under rupture loading (5).

Topographical Closed Packed (TCP) phases (Sigma and Mu) have topographically closed packed layers of atoms. These phases are detrimental to mechanical properties. The TCP phases appear as thin plates, often nucleating on grain boundary carbides, which have similar crystal structures. The structure of sigma is similar to $M_{23}C_6$ -type carbides, and Mu to M_6 -type. The extensive plate-like morphology is a detrimental source of crack initiation and propagation leading to low-temperature brittle failures (5), and to severe loss of rupture strength at elevated temperatures. To avoid the formation of these phases through chemistry control PHACOMP (for phase computation), a computer composition calculation method, can successfully be applied in alloy design (9).

2.2 STRENGTHENING MECHANISMS OF NICKEL-BASE SUPERALLOYS

2.2.1 Solid-Solution Strengthening

Nickel-base superalloys are strengthened through solid-solution strengthening in which alloying hardens both the matrix (γ) and the precipitate (γ'). The degree of hardening is related to the lattice strain and the electron vacancy number, N_v (5). γ/γ' modulus mismatch and short range order are also

suggested contributing factors to the degree of hardening (10). The effect of solid-solution strengthening is temperature dependent; as diffusion becomes important at elevated temperatures ($>0.6 T_m$) the slower diffusing elements, i.e. Mo and W, become the most effective hardeners (11). Elements strengthening the matrix are: Ti, W, Mo and to a lesser extent: Cr, Fe, Cu and Co. Elements strengthening the γ' are: Cr, Mo, Ti and Si (9).

2.2.2 Precipitation Strengthening

Precipitation strengthening is the most important strengthening mechanism in Ni-base superalloys, and is dependent upon the alloy composition and structure. In these γ/γ' alloys, factors influencing the amount of strengthening include: the size of the precipitate particles (γ'), the flow stress, the anti-phase boundary energy (discussed in the section on deformation), the volume fraction of the γ' , and the coherency strain (or misfit) between the γ and the γ' (11). Depending on the individual composition of the γ and γ' , the lattice parameters will vary. When the γ' precipitates with a different lattice parameter than the matrix then lattice mismatch (and misfit strain) develops. This lattice mismatch is expressed as:

$$\delta = 2(A_{\gamma'} - A_{\gamma}) / (A_{\gamma'} + A_{\gamma})$$

where $A_{\gamma'}$ is the lattice parameter of the γ' and A_{γ} is the

lattice parameter of the γ (4). Small mismatch and small precipitate size tend to form spherical γ' , whereas large mismatch and large precipitate size tend to form cuboidal γ' .

Gamma prime has an anomalous increase in flow stress with increasing temperature, which is important in the unique precipitation strengthening of these complex alloys. During deformation of Ni-base superalloys when dislocation movement is obstructed by the presence of precipitates, for dislocation movement to continue the dislocation must either bypass the particle or move through it by particle shear. When the dislocations are forced to pass through, or shear the precipitates, the strengthening mechanism is similar to that of γ' . The dislocation interactions which strengthen these alloys are described in the section on deformation of Ni-base superalloys (section 2.3). In general, particle shearing by dislocations is favored by large volume fraction (V_v) γ' , small interparticle spacing as well as small mismatch (11). For a given γ' volume fraction, increasing the particle size either during heat treatment or from coarsening during service corresponds to increased interparticle spacing and a tendency for bypass mechanisms (11) and a corresponding weakening of the alloy.

2.3 DEFORMATION MECHANISMS IN NICKEL-BASE SUPERALLOYS

The yield strength of high volume fraction γ/γ' superalloys remains approximately constant (or slightly increases) from room temperature to approximately 750 °C (1400 °F), the exact temperature depending upon the composition of the alloy. This unusual strength and temperature relationship is due to the drastic increase in the strength of the γ' with temperature.

At low temperatures (up to ~750 °C) these Ni-base superalloys generally deform by shearing of the γ' precipitates by planar, heterogeneous slip of dislocations (12). Dislocations shear the γ' precipitate by pairs of $a/2 \langle 110 \rangle$ dislocations on $\{111\}$ planes. These superlattice dislocation pairs (or superdislocations) occur because upon entering the ordered precipitate a dislocation disorders the structure, creating a region of antiphase boundary (APB) and thus a high energy state. The second dislocation then reorders the precipitate atomic arrangement eliminating the APB and consequently lowering the energy state. The creation and annihilation of an APB is illustrated in Figure 1 (9). The superlattice dislocation pair distance is balanced by minimizing the area of high energy antiphase boundary and maximizing the elastic repulsion of the dislocations. The $a/2 \langle 110 \rangle$ dislocations themselves may be further separated into partial dislocations. The APB energy plays an important role in deformation mechanisms. The influence of the γ/γ' mismatch is an important consideration in determining the

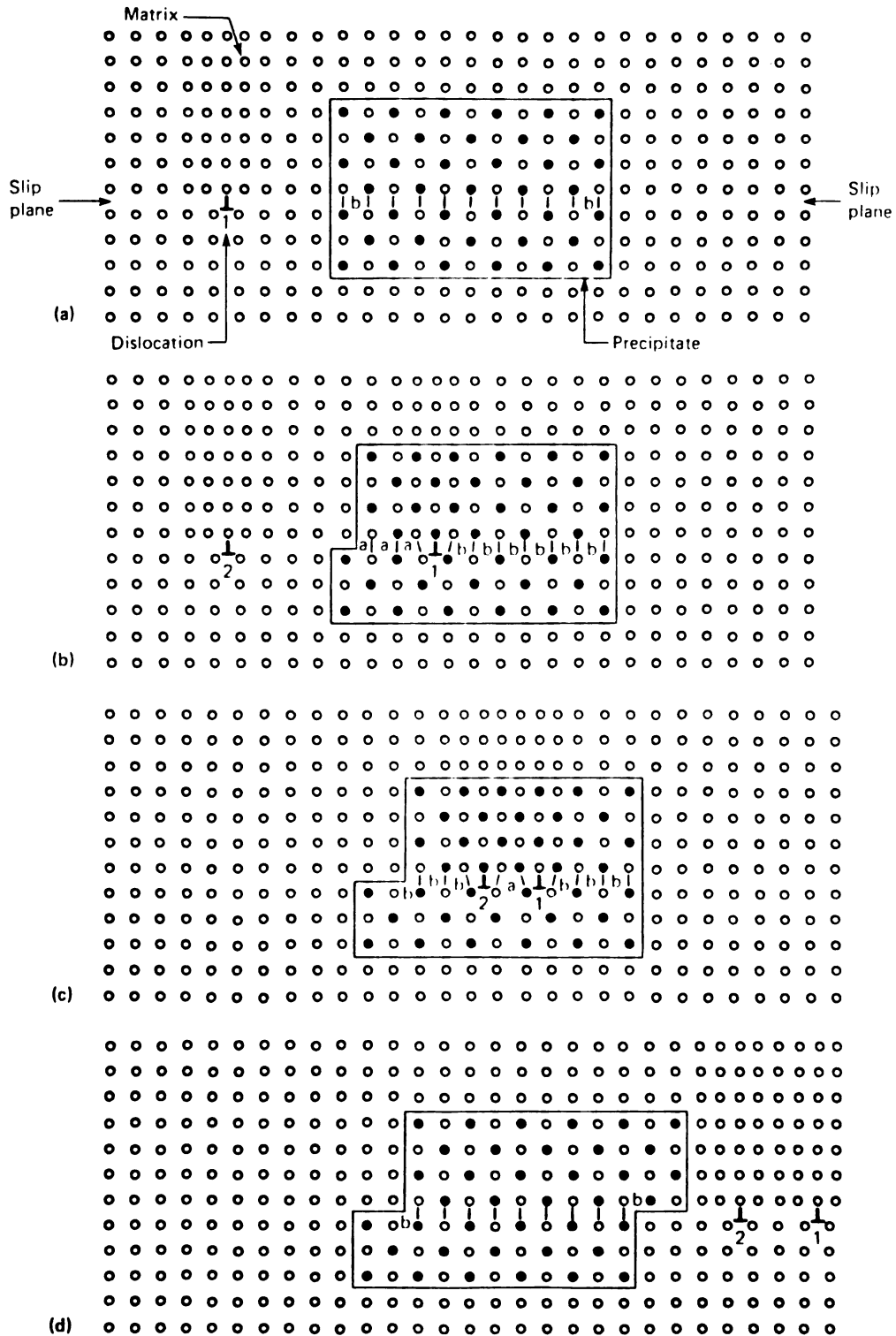


Figure 1. Schematic illustration of the creation of antiphase boundary (APB) bonds (a) formed by a dislocation moving through an ordered precipitate, and APB annihilation by a trailing dislocation (9).

mechanical properties of a Ni-base superalloy. If the γ' is precipitated such that misfit dislocations are not formed, the resulting coherency strains contribute to the APB order hardening of the γ' . This is important up to at least $0.5 T_m$ where non-diffusional deformation mechanisms predominate (4).

The anomalous increase in flow stress with temperature exhibited by γ' and its alloys (and the subtle variations in flow stress with direction and sense of applied stress) can be explained in terms of "pinning" of dissociated screw dislocation pairs by cross slip from $\{111\}$ into $\{010\}$ cube planes (13). Similar flow stress behavior of high volume fraction γ/γ' superalloys can be explained by the same cross-slip model. This cross-slip mechanism is a thermally activated process which is driven by the lower APB energy of $\{001\}$ $a/2 \langle 110 \rangle$ displacement relative to the $\{111\}$ $a/2 \langle 110 \rangle$ displacement. Screw dislocations which cross-slip onto the $\{001\}$ cube planes at intermediate temperatures ($\sim 750^\circ\text{C}$) become immobile. Similarly, dislocation pairs of edge or mixed character can take up lower energy configurations by climb (38).

The drop in yield strength at higher temperatures ($>750^\circ\text{C}$) is due to a change in the deformation mechanism from particle shearing to particle bypass and shearing. This may be ascribed to the onset of cube slip (a decrease in the cube plane friction stress) (13). The exact deformation mechanism followed, and the temperature dependencies will be governed by the composition and

structure of the alloy. Whether the γ' is sheared or bypassed, at high temperatures the associated deformation mechanisms are non-planar and very homogeneous due to the effects of easy cross-slip, climb and slip onto multiple systems (14). The temperature above which the critical resolved shear stress (CRSS) begins to drop is a function of the stress axis orientation, this is due to deformation orientation dependence. Deformation in the two phase superalloys is complicated by the presence of γ/γ' interfaces and variations in the size, distribution and morphology of the γ' phase (13).

2.4 MICROSTRUCTURAL INSTABILITIES

Since superalloys are very complex, they are not in thermodynamic equilibrium, elevated temperatures and/or high mechanical stresses can cause microstructural changes. One such change has already been discussed, that is the breakdown of primary MC carbides in the reaction: $MC + \gamma \rightarrow M_{23}C_6 + \gamma'$. The matrix stability decreases as Co, W, Mo, Ta and Cr increase in the matrix. This is due to the increased tendency to form detrimental TCP phases, when the material is alloyed beyond its solubility limits (4). Another instability reaction which can take place is the coarsening (ripening) of the γ' precipitate.

Elevated service temperature will cause the γ' precipitate to coarsen, or increase in size (5). Isothermal coarsening

results in the development of rods or plates aligned along the cube direction on a local scale, with a decrease in short range elastic strain and system surface energy (4). Coarsening of this type results in increased interparticle distances which allow dislocation bypass mechanisms to operate instead of particle shearing. This coarsening is detrimental to the strength properties (15). The stability of the γ' size and shape is related to the mismatch, temperature and stress (4).

The sense and size of the mismatch is dependent on the alloy composition, and temperature of the alloy (the thermal expansion of the $\gamma' < \gamma$) (4). Negative mismatch leads to the development of plates, whereas a positive mismatch tends to develop rods. Plates are more desirable than rods (4). As previously mentioned, misfit coherency strains have important strengthening effects in γ' . But it is also known that strong coherency strains (large mismatch) are the driving force for coarsening (4, 5), and that minimizing this coarsening will help to retain long time creep resistance and strength properties (5). Scarlin reports (15), for fatigue testing of Ni-base superalloys (IN 738 & IN 939) before and after high temperature exposure, the coarsening caused a decrease of approximately 25% in the hardness and ductile tearing along softened grain boundary zones of coarsened γ' .

A beneficial effect of γ' coarsening occurs when rafting or fine lamellar γ' structures are produced during coarsening under

an applied load, or strain-aging (4, 16). The rods or plates align perpendicular or parallel to the direction of applied stress, depending on the crystalline orientation and sense of misfit. When the lamellar structure is perpendicular (rafting) to the applied stress, dislocation blockage occurs and particle cutting must take place (4, 14, 16). Excellent long time creep-resistance has been achieved by strain aging superalloys (42).

2.5 OXIDATION OF NI-BASE SUPERALLOYS

Elevated-temperature oxidation resistance in superalloys is based on selective oxidation (17, 18) processes in which very stable oxide layers develop, preventing further oxidation. The surface stability is critically dependent upon forming and maintaining continuous, protective oxide scales on the surfaces of these alloys. Degradation is therefore dependent on factors that damage these scales and mark their subsequent redevelopment improbable (19).

Superalloys can exhibit a wide range of oxidation behavior, but generally can be categorized as either chromia formers (Cr_2O_3) or alumina formers (Al_2O_3) depending primarily upon the alloy composition (18, 19). Whittle (18) summarizes that Ni-base superalloys will be chromia formers if there is greater than or equal to 15% Cr and less than or equal to 5% Al, and alumina formers for alloys with greater than 5% Al and greater

than 5% Cr. Felix (20) states that the type of scale formed depends primarily on the Cr/Al ratio. He suggests that 4 is the critical ratio of Cr/Al, above which chromia forms. For Mar-M 247 this ratio is $8.25/5.5 = 1.50$, making it primarily an alumina former. This is consistent with oxide scales on Mar-M 246 (a sister material to Mar-M 247 with a Cr/Al = 1.50 also), which were found to consist of a complex oxide outer layer (Cr_2O_3 and Al_2O_3) and an inner layer of Al_2O_3 (18). Felix (20) also suggests that alloys with the Cr/Al ratio greater than 10 have a tendency for preferential oxidation attack at grain boundaries, largely due to the grain boundary carbide network M_{23}C_6 , where M is usually Cr. Alumina scales are typically considered more oxidation resistant because the chromia scales become gaseous oxides, or volatile, at temperatures above approximately 900 C (17, 19), and because of the slower growth (or diffusion) rate of alumina (18).

The development of the protective scales are not immediate (17, 18, 19). Transient oxidation in which less protective oxides of essentially every reactive component forms first. The continuous protective scales formed beneath the transient oxidation products. This is shown schematically in Figure 2 (19). The products which form vary depending upon the underlying phases. In general, increased formation of transient products leads to poorer oxidation resistance.

Not all phases in superalloys are chromia or alumina

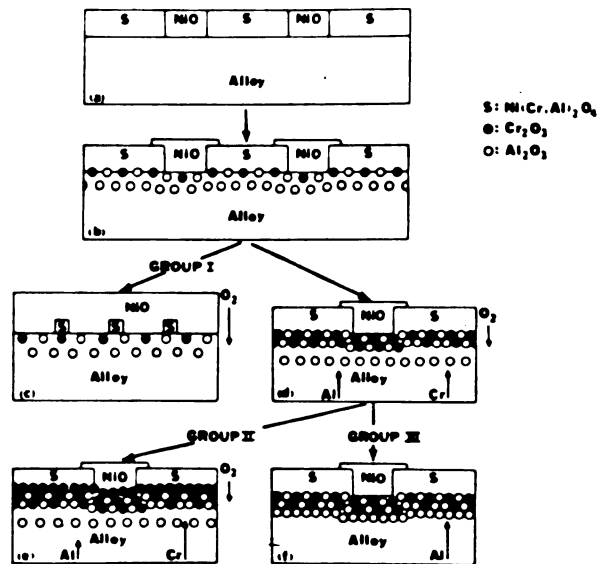


Figure 2. Schematic diagram illustrating the sequence of steps that take place during the development of NiO (Group I), Cr₂O₃ (Group II) and Al₂O₃ (Group III) scales on Ni-Cr-Al alloys. The amount of transient oxides formed prior to the development of a continuous layer of a given oxide depends upon the alloy composition (19).

formers. Those phases which do not have sufficient concentrations of Al or Cr are preferentially attacked. Pettit and Meier (17) conclude that in all superalloys, carbides, when present, are preferentially attacked (17). The only protective scale that can be formed over the carbides is chromia and often this scale is not protective due to cracking (17). Carbides in superalloys are therefore sites of excessive oxidation. Harris et al have postulated that DS CM 247 LC, a chemically modified form of Mar-M 247, may show some advantages in terms of coating life due to smaller script-type carbide colonies compared to DS Mar-M 247. These carbide "rosette" patterns are often associated with coating breakdown (21).

Cyclic oxidation conditions, whether due to cyclic temperatures, thermal stresses, and/or cyclic wear conditions can result in a breakdown of the continuous protective scale. The scale can become cracked, with spalling (17, 18, 19) and physical wear removing the protective oxide scale. Under the appropriate conditions the scale builds up again and under cyclic conditions is then removed again. Continuation of these processes eventually causes a depletion of the Cr and Al in these regions to the extent that the protective scales can no longer be redeveloped and more rapid, less protective oxidation results (17, 18, 19). The eventual depletion of the Cr and Al results in a zone denuded in γ' beneath the oxide scale (19), which weakens the material (18).

Internal oxidation, either preferential phase or grain boundary oxidation, is a problem because it reduces load bearing capacity and imposes stress concentrators. Grain boundary oxidation processes have been major problem areas in elevated-temperature fatigue testing; the fatigue crack propagates intergranularly at a faster rate than it does transgranularly.

Two possible mechanisms of environmental damage include, the formation and cracking of an oxide, and the embrittlement of boundaries through oxygen accumulation (22). Grain boundaries are the easiest paths for oxygen to move along (23). Rather than oxide cracking, it is possible for crack formation to occur as a result of oxygen pick up and subsequent embrittlement of grain boundaries. This macroscopic oxidation occurred after microcracks had formed (22). Cracking is fundamentally associated with environment. A study of dynamic environmental interactions would appear to be important in order to give a better understanding of high-temperature low-cycle fatigue (HTLCF) in Ni-base alloys (22).

Elevated-temperature diffusion coatings, or "aluminized" alloys are covered widely in the literature (24, 25). These treatments are based on creating a high concentration of Al on the surface (i.e. as NiAl) which then forms an aluminum-rich oxide. If the high-temperature coatings are not adequately suited for the system, they can decrease the fatigue life by cracking and introducing early crack initiation sites on the

specimen.

2.6 DIRECTIONAL SOLIDIFICATION

The theory of solidification and structure control of superalloys is covered by Cole and Cremisio (6). They define an interface shape determiner (ISD) which is described by the equation:

$$ISD = G/V - FR$$

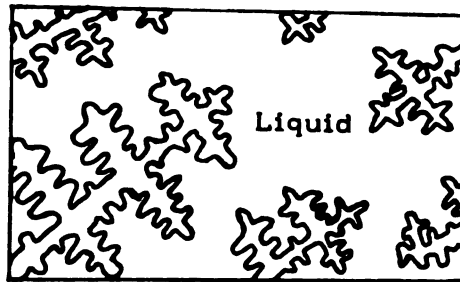
where G is the temperature gradient in the liquid at the interface, V is the freezing rate, D is the diffusion coefficient of solute in the liquid and FR is the freezing range. When ISD is positive, the interface between solid and liquid is basically smooth and plane front growth occurs, when ISD becomes negative dendrites evolve.

Most superalloys freeze over a large freezing range ($ISD \ll 0$) such that the cast structure is inherently dendritic. A dendrite is composed of a primary arm, and crystallographically similar secondary and tertiary arms, etc. In FCC alloys, dendrites grow in the $\langle 001 \rangle$ directions.

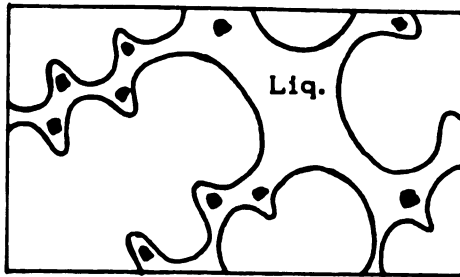
The complex segregation pattern associated with dendritic growth is one of the pervading features of superalloy solidification. Solutes that lower the melting point of the alloy

(i.e. Cr, Al, Ti, Ni, C) segregate to interdendritic regions, and solutes that raise the alloy melting point (W, Co, Ta, Hf) solidify within the dendrite center, leaving the interdendritic regions low in these elements. The proposed solidification sequence as shown in Figure 3 (26), illustrates the segregation associated with dendritic growth, carbide formation and eutectic formation. A detrimental feature of intergranular segregation occurs when segregates form nearly continuous layers of second phases; these boundaries can be readily fractured during an applied stress (6).

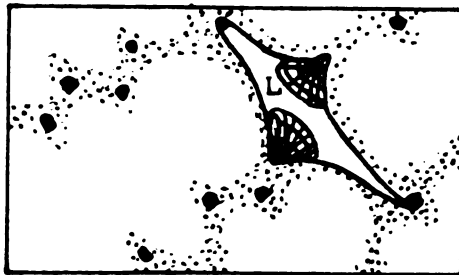
Directional solidification (DS) component casting technology was pioneered by Pratt & Whitney Aircraft and was developed to achieve significant increases in creep strength (temperature capability), thermal fatigue properties and component durability (21). These columnar grained dendritic castings eliminate the inherent defects which are associated with grain boundaries oriented normal to applied stresses. Columnar grains develop under conditions of relatively high thermal gradients and the flow of heat is unidirectional from the liquid through the solid (grain nucleation is prevented in the bulk liquid). For DS columnar grain castings the heat-flow direction must be oriented axially (6). The formation of columnar grains with [001] orientation, and the principle of directional solidification are shown schematically in Figures 4 (9) and 5 (27).



γ' dendrites



MC carbides



γ/γ' eutectic



Borides & modified matrix

Figure 3. Proposed solidification sequence illustrating segregation associated with solidification (26).

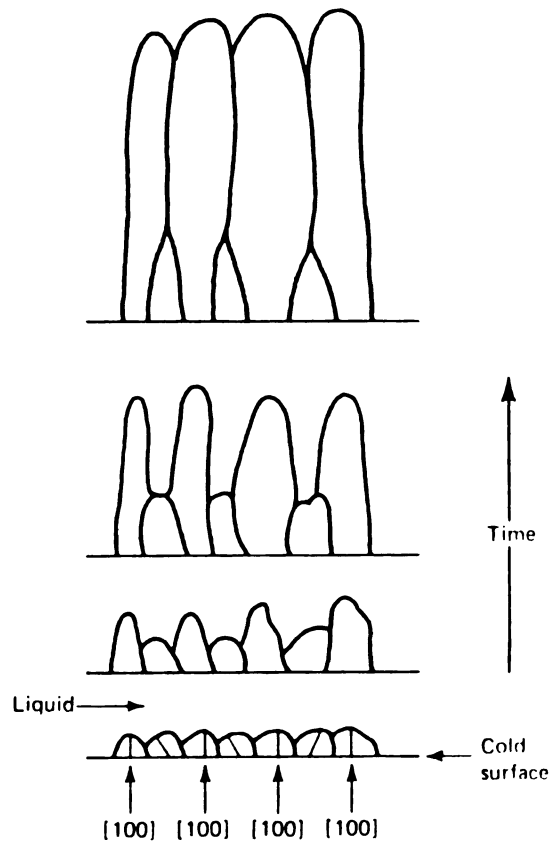


Figure 4. Schematic illustration of the formation of columnar grains having [100] orientation. Each columnar grain is oriented randomly about the vertical axis (9).

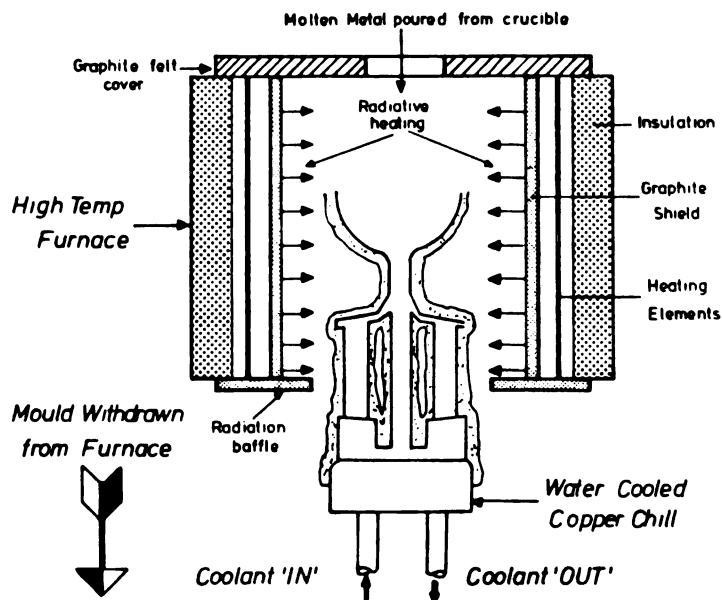


Figure 5. Principle of directional solidification (27).

Creep voids form around $M_{23}C_6$ carbides on grain boundaries normal to the stress axis (6). When these grain boundaries are absent the creep resistance is improved. Thermal fatigue resistance is improved because the Young's modulus (E) is approximately two thirds that of conventionally cast alloys of the same material, hence the thermally induced stress is less; $\Delta\sigma = E\alpha T$, where α is the coefficient of thermal expansion and T is the temperature (28). Oxidation and hot corrosion resistance is improved because grain boundaries are paths of preferential attack and have high diffusion rates. Directional solidification is beneficial in thin walled castings where the rupture life of conventionally cast (CC) alloys decreases with decreasing section thickness (modern cooled turbine blades) as the probability increases that a transverse grain boundary may extend through the specimen thickness (28). In CC materials, crack growth rates normal to the solidification direction are found to be much higher.

Single-crystal materials have the best properties since all grain boundaries can be eliminated, and the grain boundary strengthening elements (C, B, Hf, Zr) can also be eliminated. These elements are melting point depressants, hence higher solutionizing temperatures can be used (29); and the γ' can be completely dissolved and re-precipitated as a fine dispersion of γ' (16). Coarse γ' particle sizes result in a significant reduction of rupture strength (29) and other properties already mentioned. Higher service temperatures can also be used,

increasing the efficiency of the system.

2.7 FRETTING

Fretting is a process in which material is removed from one or both of two contacting surfaces when the surfaces undergo cyclic tangential displacement with respect to each other (30). Accumulation of fretting debris is one of the distinguishing features of fretting wear (31,32) and accounts for the majority of surface damage (33). This wear debris is heavily work hardened and oxidized; a condition that results in three-body abrasion (31, 32). The roughening of the metal itself that is associated with the fretting product, may vary from patches of microscopic pits to large, shallow abraded areas (34). The main damage of fretting is usually the degradation of the surface finish and/or the initiation of fatigue cracks (30).

Fretting involves a number of factors such as contact between surfaces, frictional effects, adhesion, wear, surface fatigue, stress concentrations, corrosion and environmental effects, all of which are major subjects in their own right (35). Fretting wear processes are extremely complex (31, 36) and not well understood (30), especially at elevated temperatures. Several important fretting theories have been reviewed by Hoepfner (37). Fretting theories include "molecular attrition", cohesion, adhesion, chemical and mechanical abrasion

(31). Barwell (38) concludes that fretting is initiated by adhesion, amplified by corrosion and has its main effect by abrasion. Hurricks (31) describes the mechanisms of fretting to occur in three stages: an initial stage of adhesion and metal transfer, a second stage of debris generation of a mechanico-chemical nature, and finally a steady-state stage of disintegration and dispersal of zones affected by initial stages, resulting in a mixture of debris and metal in wear contours.

Hondros (39) discusses the Bowden-Tabor theory of friction which attempts to explain the initial stage of fretting, adhesion and metal transfer. Practical surfaces are usually covered by oxide films and are of such roughness on the atomic scale, that only a tiny fraction of the contacting area (approximately 1/1000) at the peaks of asperities is the real area of contact (39) and is subjected to powerful adhesive forces (32, 40). When the load is borne by a few asperities the localized pressures are so great the summits of the asperities are deformed plastically. Pressure welding occurs to produce tiny continuous metallic junctions between the surfaces (39). The metal-to-metal junction is sheared by frictional motion and a small fragment becomes attached to the other surface. Sliding continues and the fragment is transferred again, increasing in size (38). This element grows to a size that supports the load, becoming the only contact and continuing to grow.

One of the interesting forms of wear debris found in

certain fretting situations is spherical particles. Hurricks (41) states that it is somewhat surprising that the characteristically non-uniform processes and continuously variable conditions that exist at interacting surfaces during fretting should produce anything as geometrically near-perfect as spheres. Yet there are a number of reports in the literature detailing the occurrence of spherical wear debris (38, 42-45). Hurricks (41) concludes that spherical particles can form during fretting wear if the appropriate experimental conditions prevail. Typically an adhesive situation is required and an alternating form of deformation initiating the formation and growth of the spheres, either at the specimen surfaces or within tears or fissures, is present in the adhesion zones. The largest spherical particles were found at higher fretting temperatures, where the wear surfaces develop into a more plastic state under the applied fretting conditions (440 & 500 C, mild steel (41)).

High temperatures can be achieved during sliding between metal surfaces and localized "hot spots" have been proven (39). As energy is dissipated under fretting conditions, plastic deformation has been seen and increases in local temperatures have been suggested which may amount to several hundred degrees centigrade (35). Barwell (38) describes the "flash temperature" to be the excess in temperature, caused by friction, over the bulk temperature. The high temperatures which may arise at fretting contacts can promote surface oxidation (31) or change the nature

of the oxide (36).

As previously mentioned high-temperature oxidation resistant superalloys and other alloys (32, 39) at elevated temperatures form protective adherent oxide films (46). Initially the surface formed oxide prevents metallic contact and adhesion (31), thus reducing the coefficient of friction. If the fretting amplitude is large enough the oxide layer can be disrupted (31). The rate of repair of the oxide is thus important and this depends on such conditions as temperature, frequency of fretting motion and nature of the environment (47).

For Ni-base alloys, a temperature has been found above which there is a reduction in the coefficient of friction and a corresponding lowering of the wear rate (47, 48). Wood et al (48) attributes these reductions to the formation of a "glaze" on the rubbing surface. The appearance of the "glaze" was described as showing many distinct, well formed small abrasion grooves in the main load bearing areas, parallel to the sliding direction. The "glaze" had a glassy appearance, but displayed a well defined electron diffraction ring pattern (polycrystalline), and was found to consist of simple oxides. The formation of the "glaze" is thought to be due to the contact pressures and high localized temperatures in the load bearing regions, causing thermal softening at points of contact between oxide particles resulting in a sintered compact mass (47). Wood (48) suggests that the contact pressure and very high localized temperatures

attained in the load bearing regions may even result in melting at points of contact followed by resolidification. A proposed mechanism of "glaze" formation is as follows: initial sliding occurs with a large amount of tearing and deformation thus removing the thin oxide layer, then transient oxidation forms (aided by plastic deformation); next removal and build up of transient oxides with sliding occurs until a stable oxide layer is formed, then localized temperatures cause thermal softening giving rise to a thin, physically homogeneous "glaze". Once the thermally softened layer is established, a drop in friction occurs; virtually all the surface damage occurs before the "glaze" forms (48).

2.8 FATIGUE

The most common cause of damage to engineering components is caused by fatigue (49). Fatigue leads to fracture under repeated or fluctuating stresses having a maximum tensile value less than the tensile strength of the material. Fatigue life (N_f) is the number of cycles of stress that can be sustained prior to failure for a given test condition. Fatigue tests attempt to simulate stress or strain conditions developed in machine parts by vibration of cyclic loads (50). Fatigue tests are also used to study the effects of oxidation and corrosion, surface conditions, temperature, size, and stress concentrations in relation to the fluctuating loads (50). Fatigue of Ni-base

superalloys has been extensively studied. A review of fatigue behavior in Ni-base alloys is given by Gell and Leverant (51), other reviews are also given (11, 12, 14, 52, 53).

The fatigue process involves the initiation and propagation of a crack or cracks to final fracture. Fatigue cracks usually initiate at the surface where stresses are highest and corrosion and changes in the geometry exist (54). Fatigue cracks generally propagate in a transgranular manner, but can also propagate intergranularly. Intergranular cracking usually occurs at elevated temperatures due to oxidation and diffusional effects along the grain boundaries, and is a faster crack propagation mode than transgranular cracking.

Transgranular fatigue crack growth is characterized by two stages of crack propagation. These two stages are called Stage I and Stage II and are shown schematically in Figure 6 (54). Stage I mode of crack growth usually initiates at surface discontinuities and grows in a plane of maximum shear stress. Stage I crack growth is generally small, propagating in a zone of one or two grains (49). Stage II crack growth follows Stage I with the crack propagating along planes of maximum tensile stress.

Transgranular cracking of Ni-base superalloys originates at the surface and displays an extensive Stage I crack propagation mode (51). The Stage I cracking in these superalloys usually

occurs along crystallographic slip planes, due to the deformation in coarse planar bands. Stage II cracking is usually non-crystallographic due to the homogeneous deformation mode and occurs approximately normal to the stress axis (51). The fatigue behavior of Ni-base superalloys is related to the deformation characteristics which are dependent on variables such as alloy composition, microstructure, strain rate, stress conditions, and temperature.

2.9 FRETTING FATIGUE

In jet turbine engine blades, a crack initiated from fretting surface damage may propagate to failure if the alternating bending stress due to turbine blade vibration is large enough (55). The resulting failure is said to be due to fretting fatigue. Fretting fatigue is defined as the decrease in fatigue life due to fretting surface damage (46). Fretting fatigue can drastically reduce the fatigue strength (31, 47), with reductions up to 50% being reported by Benson (56). Fretting damage caused by stress risers can cause catastrophic failures by fatigue (32). There is very little information published on fatigue behavior at high temperatures in the presence of fretting. Figure 7 is a systems diagram illustrating the numerous factors affecting fretting fatigue (37).

It is generally accepted that one of the major factors in

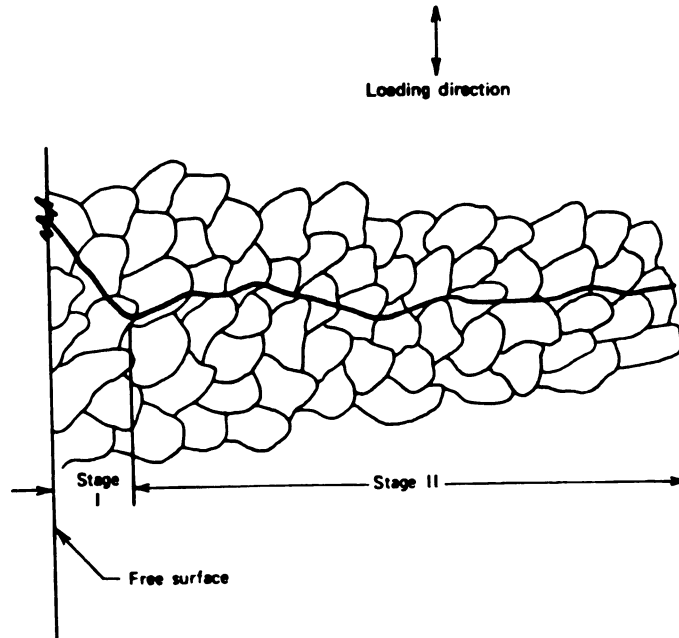


Figure 6. Stage I and Stage II modes of transgranular fatigue crack growth (54).

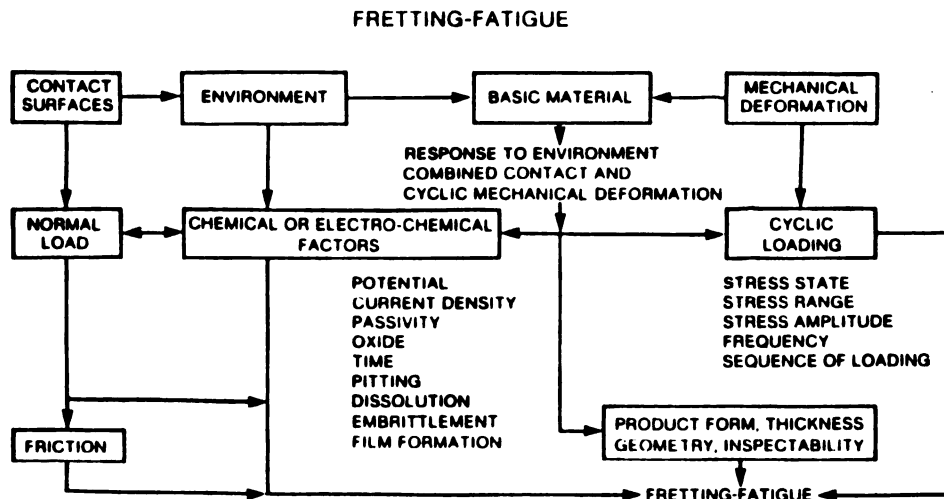


Figure 7. Systems diagram illustrating numerous factors in fretting fatigue (37).

the initiation of fatigue cracks during fretting is the presence of alternating shear stresses in the surfaces arising from frictional forces associated with oscillatory movement (35). Maximum frictional stresses on a fretted surface are concentrated at the edges of the contact region, and cracks are generated near this slip/no-slip area (57). Crack initiation from near the slip/no-slip boundary is mentioned in several reports (35, 48). A fretting fatigue damage threshold has been reported (37) above which the fretting contact has little effect on the subsequent fatigue life. Hoepfner et al (37) states that after Stage I fatigue crack is initiated from fretting damage, the fretting plays no further role in the propagation of the fatigue crack. Yet the environment may influence the fatigue crack propagation life (37).

Shot peening is one technique commonly used to improve resistance to fretting fatigue. Shot peening increases the hardness of the specimens' surface, depending upon the work-hardening capacity of the material (55), and introduces beneficial residual compressive stresses (35, 48, 55, 56). These residual stresses serve to retard the propagation of incipient fatigue cracks. Taylor (47) reported that fretting decreased the fatigue strength by 60%, but that shot peening gave improvements of 40% on the degradation due to fretting.

2.10 REPLICATION

A replica is a close reproduction or facsimile of a surface which is to be examined microscopically when the original specimen can not be directly studied. Replicas may be taken of specimens that are: too large to fit into the microscope, too valuable for direct examination, not able to be removed from the field, or when observing surface changes over a period of time (such as recording the progression of wear). Replicas are used as a form of data storage (58). Replicas are commonly examined by scanning electron microscopes (SEM) and transmission electron microscopes (TEM). Since the majority of research conducted in this thesis relates to replication of surface structures for scanning electron microscope studies, the following introduction to replication will concentrate on SEM techniques.

The basic requirement of replication is that the materials used must accurately reproduce the original surface. Not only is the reproduction of detail important, but the expertise required from the operator and the time involved to produce a replica are considered key factors (59). Characteristics that a good replicating medium should possess include: good wetting properties (or low surface tension), rapid polymerization without shrinkage, easy detachment from the surface without distortion, and resistance to vacuum, irradiation and heat (60).

Replicas can be single-stage or two-stage. Single-stage

replicas consist of the impression being made in one step, resulting in a negative copy. When the negative replica is examined the image is reversed. This type of image can be very confusing as both the relief and direction are reversed. Some SEMs have image inversion, an electronic signal processing device which can produce the original perspective (60). If the SEM does not contain this device then a two-stage replica should be made to display the correct image. A two-stage or positive replica is made by replicating the negative replica, thus the negative becomes a mold for the positive.

Two types of replicating media are commonly used for SEM negative replication. Cellulose acetate replicating tape (also used for TEM studies) and dental impression media. The cellulose acetate replicating tape is available in roll form from electron microscope suppliers. The tape is 1" wide with a variety of thicknesses (0.022 - 0.127 mm). Acetylcellulose sheets (10 x 12 cm with a thickness of 0.08 or 0.034 mm) may be used for large areas. Very sensitive elastic dental impression materials have been developed, are available from dental supply companies, and have been adapted for materials research. Impression media have been used for replicating surfaces which can not be replicated with cellulose acetate, such as very large surfaces and rough or hard-to-reach surfaces. The techniques used with these types of replicating media are described in detail by Gabriel (60).

The choice between types of replicating media is based on several factors: fineness of surface structures, size and shape to be replicated, ease of access, etc. Cellulose acetate, although limited in size, supposedly has better resolution at higher magnifications than dental media (60). Yet for two-stage replicas, Pameijer (59) has introduced a dental precision impression material, Reprosil, which in combination with low-viscosity resins has produced superior replicating results over other techniques. Reprosil is an addition cured vinyl polysiloxane elastomeric impression material which is non-toxic and non-irritant (59). Reprosil will remain dimensionally stable for several days. This can be important in making replicas because the time for pouring the positive replica is not critical. The Reprosil is easily removed from the specimen and from the positive resin replica, depleting the possible problem of the negative replica contaminating the positive. Because of its elastic memory the Reprosil will return to its original cured state when peeled off undercuts or curved shapes. Pameijer (59) found the combination of Reprosil and Spurr's low-viscosity embedding medium (resin) had the best reproduction of detail and was the most versatile method tested in a study comparing replication techniques.

CHAPTER 3

MATERIALS AND EXPERIMENTAL PROCEDURES

3.1 MATERIALS

Fir-tree attachment specimens and loading fixtures (specimen grips) were produced in the same manner and with the same geometries as turbine blade attachments and corresponding disk areas of the F109 jet turbine engine (Figure 8). The materials were supplied in their finished form by Garrett Turbine Engine Company, see Figure 9.

The alloy used to make the test specimens was MAR-M 247 DS, a directionally solidified Ni-base superalloy. The composition is given in Table 1. Specimens were machined from investment castings produced by TRW Aircraft Components Group. The fir-tree attachment shape was produced by very accurately shaped grinding wheels. The specimens had $\langle 001 \rangle$ longitudinal orientations, with a specified maximum allowable deviation of the columnar grains from the longitudinal axis of 10 degrees (20 degrees maximum angle on intersecting columnar boundaries). The cooling rate during crystal growth was not specified by Garrett, but was reported to be approximately 100°F/minute from the

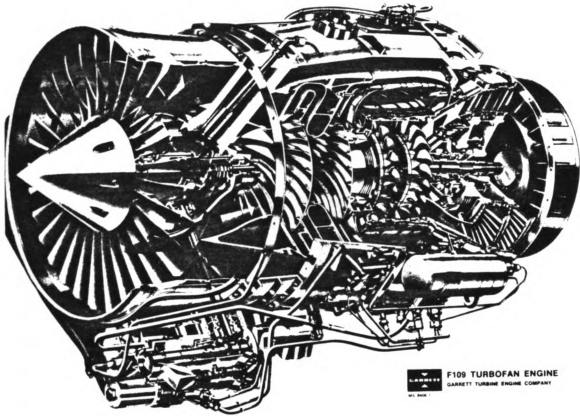


Figure 8. The F109 jet turbine engine.



Figure 9. Fir-tree attachment specimen and loading fixtures.
0.4 X

solution temperature. The heat treatment schedule performed, simulating blade heat treatment, was as follows:

Solution Treatment: 2230°F for 2 hours, rapid inert gas cool to below 1800°F, air cool to room temperature (RT)

Simulated Coating Cycle: 1800°F for 5 hours.

Aging Treatment: 1600°F for 20 hours, air cool to RT

After machining, the entire specimen surfaces were shot peened to introduce surface residual compressive stresses which inhibit crack propagation.

The alloy of the specimen loading fixtures was Astroloy; the composition of which is also given in Table 1. The specimen grips, or loading fixtures, were also ground to precise tolerances, thus duplicating the disks blade receiving geometry. The heat treatment schedule for the fixtures simulated the disk heat treatment and was as follows:

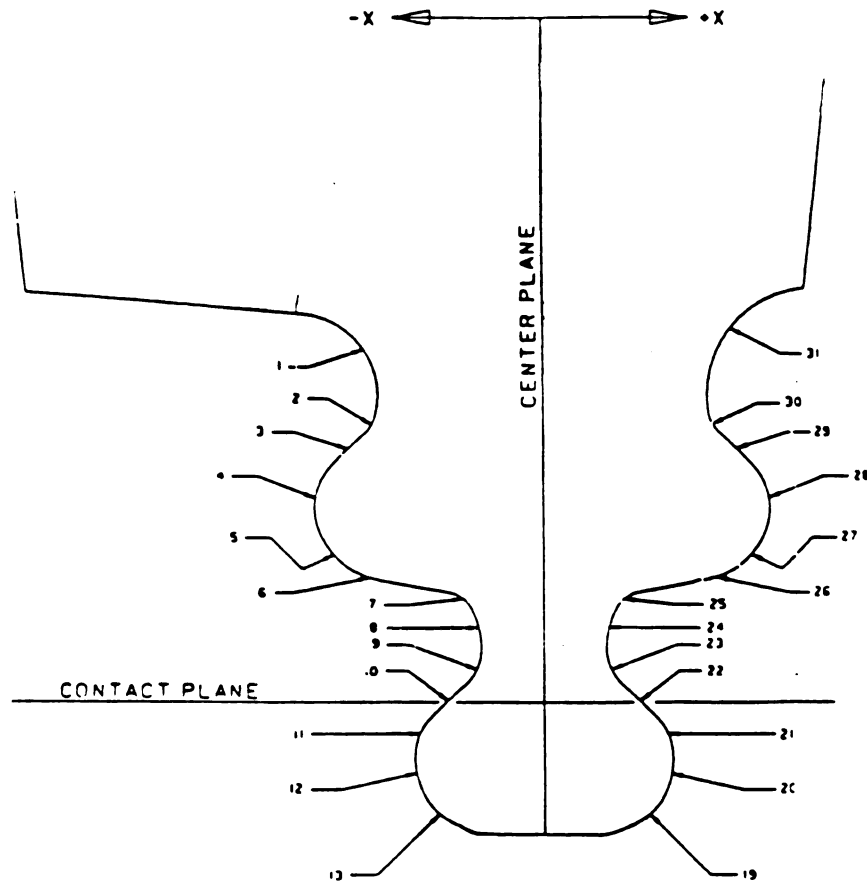
Solution Treatment: 1975-2075°F for 4 hours, quench into molten salt bath at 600-1000°F.

Aging Treatment: 1600°F for 8 hours, air cool to RT,
1800°F for 4 hours, air cool to RT,
1200°F for 24 hours, air cool to RT,
1400°F for 8 hours, air cool to RT.

3.2 SPECIMEN GEOMETRIES

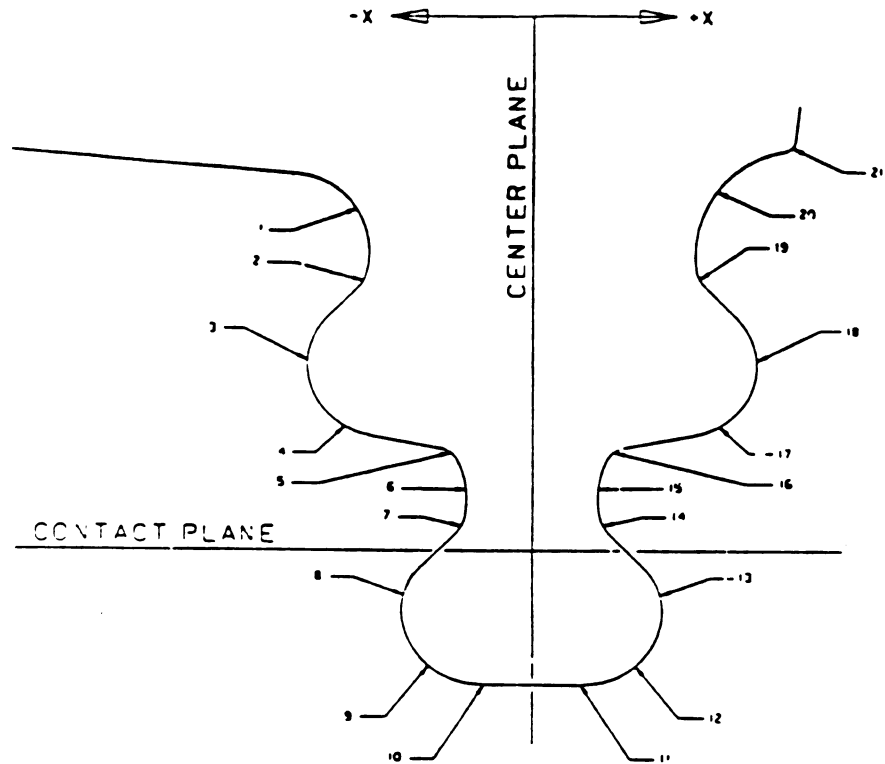
The two-tang (or hook) fir-tree test specimens were supplied with two different specimen geometries, flat and crowned. These two test geometries are identical with the exception of the load bearing surface. The flat geometry specimens have planar load bearing surfaces, while the crowned specimens have curved load bearing surfaces. Specimen specification (crowned) are shown in Figure 10 (61). Loading fixtures have planar load bearing surfaces. Their specifications are shown in Figure 11 (61). The current design geometry has planes for the load bearing surfaces in both the blade fir-tree area and the turbine disk attachment area. Theoretical data compiled by Garrett (65) based on surface stress studies indicate a possible 10 fold increase in fatigue life for the crowned geometry.

The specimens and loading fixtures are asymmetric about the longitudinal or stress axis. The turbine blades, and thus the test specimens, are designed with the asymmetry to provide an extended shoulder of supporting material for the trailing edge of the blades. The hooks of the fir-tree are symmetrical. The turbine blade asymmetry is shown in Figure 12 (61).



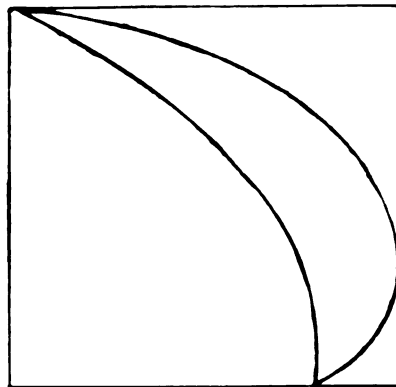
RADIUS NUMBER	-X-	-Y-	RADIUS	TOLERANCE BAND	
	CENTER PLANE	CONTACT PLANE		INITIAL	FINAL
1	-0.2747	0.2850	0.3049	0.0030	0.0030
2	-0.1789	0.2282	0.3049	0.0030	0.0030
3	-0.1538	0.2283	0.3049	0.0030	0.0030
4	0.0712	-0.0313	0.3049	0.0030	0.0030
5	-0.1200	0.1438	0.3049	0.0030	0.0030
6	-0.1097	0.1475	0.3049	0.0030	0.0030
7	-0.1039	0.1547	0.3049	0.0030	0.0030
8	-0.0725	0.0589	0.3049	0.0030	0.0030
9	-0.1107	0.0403	0.3049	0.0030	0.0030
10	-0.0827	0.0401	0.3049	0.0030	0.0030
11	-0.0714	-0.0000	0.3049	0.0030	0.0030
12	0.1442	-0.2157	0.3049	0.0030	0.0030
13	-0.0537	-0.0385	0.3049	0.0030	0.0030
14	-0.0338	-0.0413	0.3049	0.0030	0.0030
15	-0.0471	-0.1483	0.3049	0.0030	0.0030
16	0.0471	-0.0483	0.3049	0.0030	0.0030
17	0.0338	-0.0413	0.3049	0.0030	0.0030
18	0.0537	-0.0385	0.3049	0.0030	0.0030
19	-0.1442	-0.2157	0.3049	0.0030	0.0030
20	0.0714	0.0000	0.3049	0.0030	0.0030
21	0.0827	0.0401	0.3049	0.0030	0.0030
22	0.1107	0.0403	0.3049	0.0030	0.0030
23	0.0725	0.0589	0.3049	0.0030	0.0030
24	0.1039	0.1547	0.3049	0.0030	0.0030
25	0.1097	0.1475	0.3049	0.0030	0.0030
26	-0.1097	0.1475	0.3049	0.0030	0.0030
27	-0.1039	0.1547	0.3049	0.0030	0.0030
28	-0.0725	0.0589	0.3049	0.0030	0.0030
29	-0.1107	0.0403	0.3049	0.0030	0.0030
30	-0.0827	0.0401	0.3049	0.0030	0.0030
31	-0.0714	-0.0000	0.3049	0.0030	0.0030

Figure 10. Specimen specifications, crowned geometries (61).

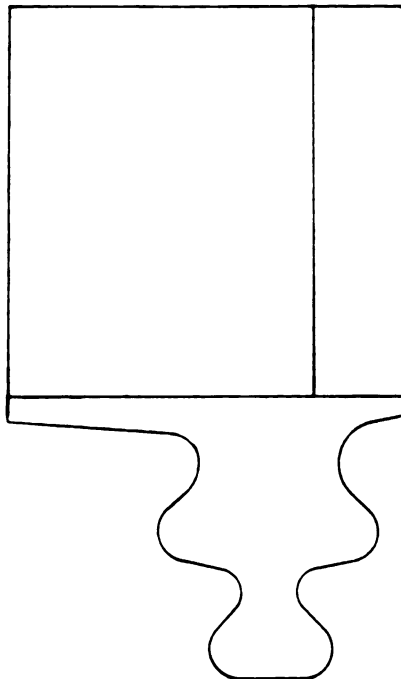


RADIUS NUMBER	-X-	-Y-	TOLERANCE BAND		
	CENTER PLANE	CONTACT PLANE	RADIUS	INITIAL	FINAL
1	-0.2878	0.2921	0.0380	0.0030	0.0030
2	-0.1773	0.2242	0.0380	0.0030	0.0030
3	-0.1563	0.2242	0.0370	0.0030	0.0030
4	-0.1188	0.1398	0.0500	0.0030	0.0030
5	-0.1111	0.1461	0.0500	0.0030	0.0030
6	-0.0724	0.0598	0.0180	0.0030	0.0030
7	-0.1148	0.0396	0.0650	0.0030	0.0030
8	-0.0795	0.3324	0.0280	0.0030	0.0030
9	-0.0714	-0.0000	0.0010	0.0030	0.0030
10	-0.0521	-0.0456	0.0463	0.0030	0.0030
11	-0.0409	-0.0428	0.0375	0.0030	0.0030
12	-0.0263	0.1005	0.2015	0.0030	0.0030
13	0.0409	-0.0428	0.0375	0.0030	0.0030
14	0.0521	-0.0156	0.0460	0.0030	0.0030
15	0.0714	-0.0000	0.0010	0.0030	0.0030
16	0.0795	0.3324	0.0280	0.0030	0.0030
17	0.1148	0.0396	0.0650	0.0030	0.0030
18	0.0724	0.0598	0.0180	0.0030	0.0030
19	0.1111	0.1461	0.0500	0.0030	0.0030
20	0.1188	0.1398	0.0500	0.0030	0.0030
21	0.1563	0.2242	0.0370	0.0030	0.0030
22	0.1773	0.2242	0.0380	0.0030	0.0030
23	0.2878	0.2921	0.0380	0.0030	0.0030

Figure 11. Loading fixture specifications (61).



Top View



Front View

Figure 12. Turbine blade asymmetry (61).

Table 1. Nominal Chemical Compositions (Wt.%)

Alloy	C	Cr	Ti	Al	Co	Ta	Mo	W	Zr	B	Hf
Mar-M247DS	0.15	8.25	1.0	5.5	10.0	3.0	0.70	10.0	0.05	0.015	1.5
Astroloy	0.06	15.0	3.5	4.0	17.0	-	5.25	-	-	0.030	-
Remainder: Ni											

3.3 EXPERIMENTAL PROCEDURES

3.3.1 Fatigue Testing

Isothermal tension-tension fatigue testing was conducted under load control in air at 650°C (1200°F) using a MTS (computer-controlled) hydraulic closed-loop machine. The frequency used for the tests was 0.33 Hz under triangular waveform from 500 lb. to 11,750 lb., and thus giving a stress ratio ($R = P_{min}/P_{max}$) of 0.44. Temperature control was achieved through induction heating using a Lepel 2.5 KW generator and induction coils formed from copper tubing. The thermocouples, close circuited to the Lepel furnace, were spot welded near the center of the specimens surface.

3.3.2 Load Train

A multi-component load train was required due to the design of the loading fixtures and the specifications of the

test program. Compressive grips were designed to accommodate and support the loading fixtures. Universal joints attached the compressive grips to the load cell and hydraulic ram. Universal joints were used to allow for orientation changes between the fir-tree ends and loading fixtures, which result from shifting and slipping of the contact surfaces. The complete load train is depicted in Figure 13 (61).

3.3.3 Fir-Tree Replicas

Fatigue testing was periodically interrupted for replication. The specimens were air cooled to room temperature under a 500 lb. load and then removed from the specimen grips. Negative replicas were taken of the entire fir-tree surfaces using Reprosil elastic impression medium. The specimens were then replaced into the loading fixtures and brought back to a 500 lb. load and 1200°F before fatigue testing was continued. Fifty-two replicas were taken from 6 specimens. Typical replicating sequences were as follows: 0, 15,000, 25,000, 35,000 cycles etc., until failure. Positive resin replicas were made from the negative Reprosil molds. The positive replicas were then prepared for scanning electron microscopy examination. This is believed to be the first application of this replication technique to materials science. A detailed explanation of the procedures along with an evaluation of the replication technique is given in Appendix C.

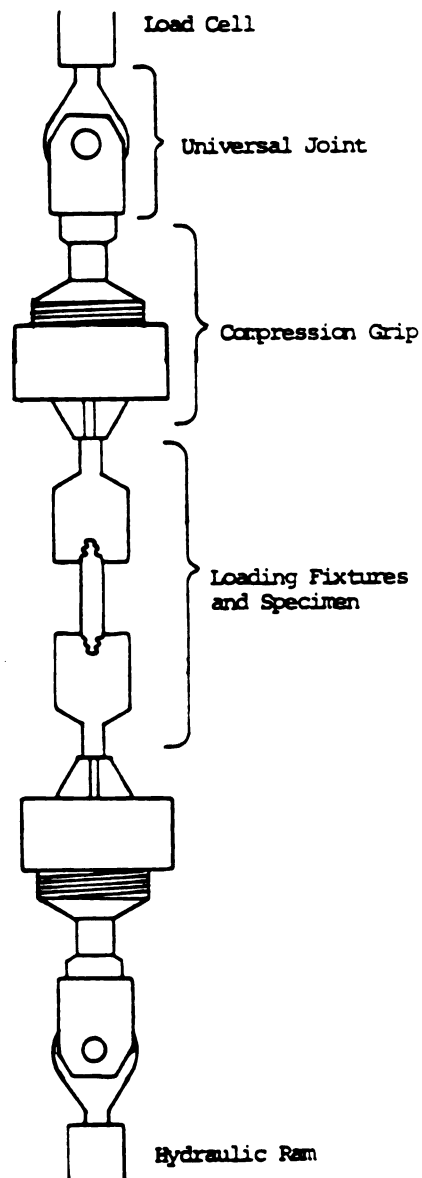


Figure 13. Complete load train (61).

3.4 MICROSTRUCTURAL EXAMINATION

Tested specimens were characterized using several different metallography techniques. Columnar grain structures were examined macroscopically after polishing and etching the unloaded surface of the specimen. Macrographs were taken with a Polaroid Cu-5 land camera and a Wild microscope.

Microstructures parallel (longitudinal) and perpendicular (transverse) to the columnar grains were examined. These samples were usually taken at the center of the specimen. Metallography sample preparation techniques are described in Appendix A. Optical metallography was conducted with a Nikon metallograph. Samples were examined in the etched and unetched conditions. Etched samples were also examined with a Cambridge scanning electron microscope operating at 20 KV. Gamma prime precipitate morphologies were examined by taking cellulose acetate replicas (RTM replicas as described in Appendix B) on transverse specimens and examining them with a JEOL 100-CX transmission electron microscope operating at 100KV.

Carbides of the MC-type with script morphologies were analytically analyzed in the unetched condition. Analytical electron microscopy (AEM) was performed on a transverse section using the dot pattern technique; this was conducted with the electron microprobe at the NASA Lewis Research Center.

Macrographs of the fracture surfaces were taken with a Polaroid Cu-5 land camera and a Wild microscope. Fractography studies were conducted on a Hitachi S-415A scanning electron microscope operating at 20KV.

CHAPTER 4

RESULTS AND DISCUSSIONS

4.1 FATIGUE DATA

The following are the results of the isothermal elevated-temperature (650°C) fatigue testing which was conducted on six fir-tree specimens. Three specimens had flat load bearing geometries while the other three had crowned load bearing geometries. Five of the six specimens were fatigue tested to failure. The bottom loading grip (grip #6) of the sixth specimen fractured during testing and the test was terminated. Two other top loading grips (#3 and #5) fractured; the initiation of the fracture cracks of these two grips appeared to be in the same location. It is believed, however, that the fracture of specimen F109-4 Cr caused the fracture of grip #5 (Figure 14), while the failure of grip #3 caused the failure of specimen F109-10 CR (Figure 15). Loading grip #4 was found to contain a crack initiating from a load bearing surface as shown in Figure 16. This crack was not found to be associated with any of the specimen failure cracks.

The specimens' fatigue lives (N_f) are listed in

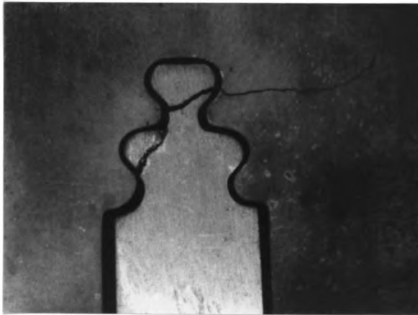


Figure 14. Specimen F109-4 Cr, A end, loading grip #5. 3.8X



Figure 15. Specimen F109-10 Cr, A end, loading grip #3. 1.55X

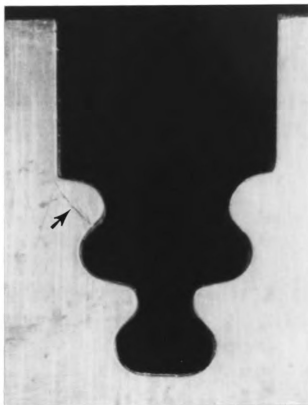


Figure 16. Loading grip #4 containing a crack initiating from a load bearing surface. 5.5X

chronological order of testing in Table 2 along with the top (T) and bottom (B) loading grips used, and the fracture initiation locations. Figure 17 illustrates the nomenclature used for describing specific locations on the fir-tree specimens and the corresponding loading grip areas. A and B indicate the specimen end, A end was always placed in the top loading grip. IN and OUT represent the inner and outer sets of hooks, or tangs, with respect to their position as they would sit in a turbine disk; the inner tangs would be closer to the center of the disk.

Table 2. Specimen Fatigue Results

Specimen	Fatigue life	T Grip	B Grip	Fracture
1. F109-14 CR	N _r : 32,564	#1	#6 (F)	-
2. F109-4 CR	N _r : 47,302	#5 (F)	#4	A _{IN}
3. F109-3 F	N _r : 11,531	#3	#4	A _{OUT}
4. F109-5 F	N _r : 19,956	#3	#4	A _{OUT}
5. F109-10 CR	N _r : 15,887	#3 (F)	#4	A _{IN}
6. F109-1 F	N _r : 51,309	#1	#4	B _{OUT}
F: Grip Fracture T: Top Grip B: Bottom Grip				

The fatigue test results give no indication of the crowned specimens having longer fatigue lives than the flat specimens. A flat specimen had the longest life (N_r: 51,309). The second longest life (N_r: 47,302) was a crowned specimen, but here the

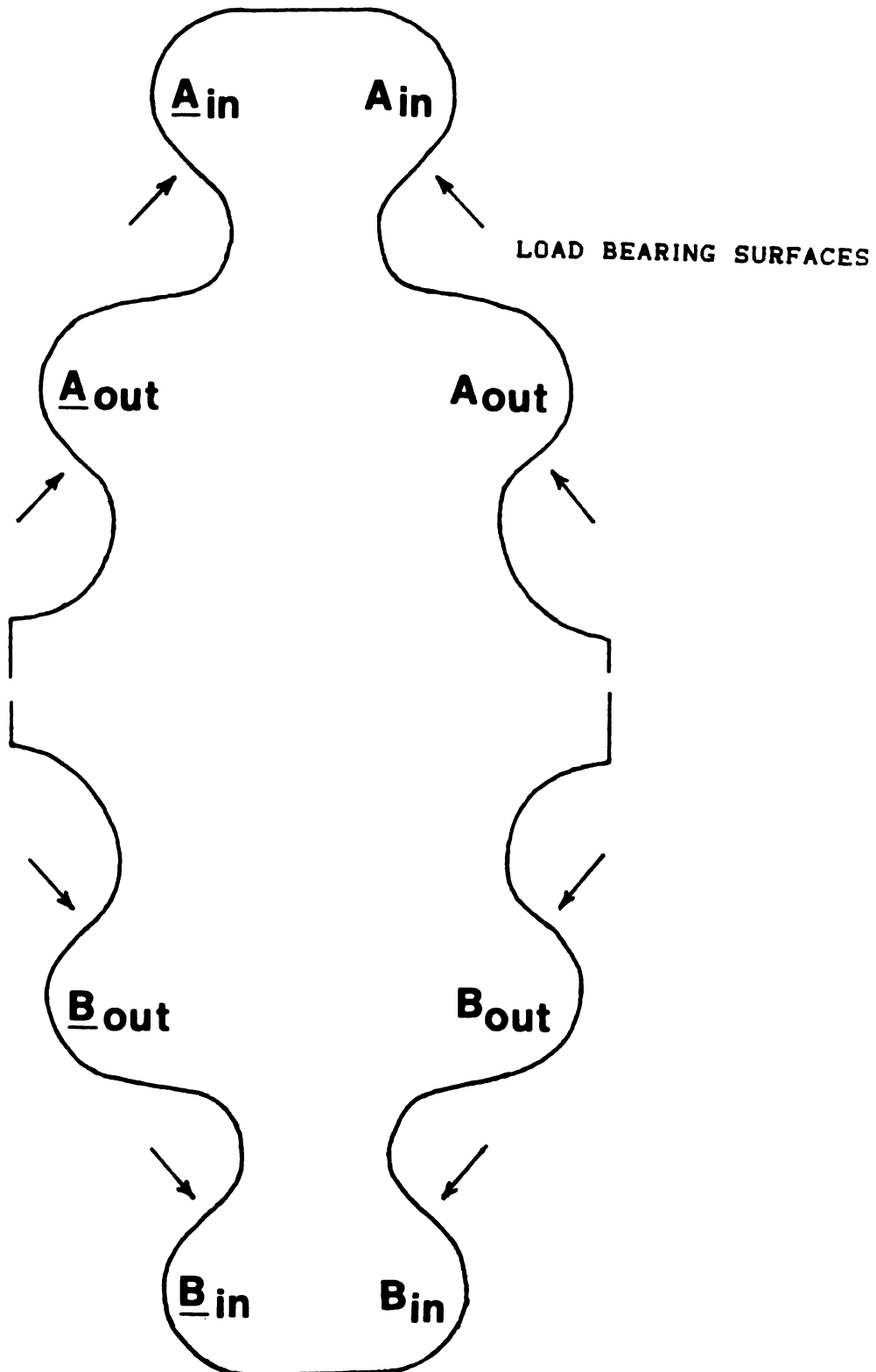


Figure 17. Illustration of nomenclature used for describing specific locations on the fir-tree specimens and for the corresponding loading grip areas.

loading grip also fractured. The three shortest life specimens all failed from the same side of the A end, and were all loaded in the same grip (#3). It is believed that the grip may have been damaged. Although grips were inspected between tests, the damage might not have been noticeable. It was found that the grips played an important role in the fatigue process, and that geometry alone does not allow for increases in fatigue life, this is due to the complex wear mechanisms which are involved.

4.2 MICROSTRUCTURAL ANALYSIS

The microstructures of the tested specimens which were examined using optical microscopy (OM), scanning electron microscopy (SEM), replica transmission electron microscopy (RTEM), and analytical electron microscopy (AEM) techniques are discussed in the following sections.

4.2.1 Dendritic Structure

The directionally solidified dendritic structures are depicted in sections longitudinal and transverse to the columnar grains, respectively shown in Figures 18 and 19. The microstructure consists of a cored dendritic structure with large script-type carbides and large γ/γ' eutectic nodular regions, primarily in the inner dendritic regions and near dendrite boundaries. The inner dendritic boundaries, or grain

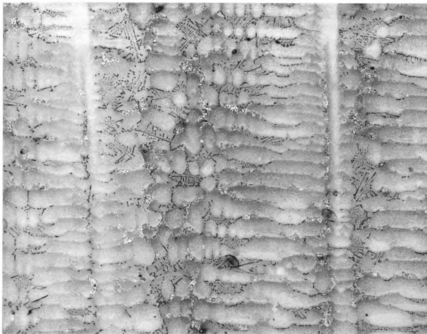


Figure 18. Directionally solidified dendritic structure sectioned longitudinal to columnar grains. OM 50X

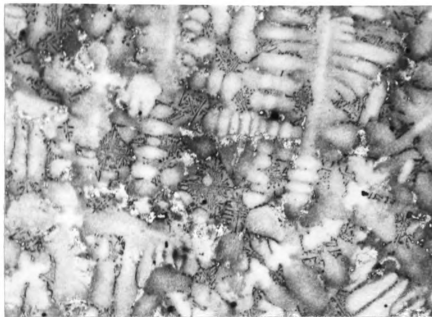


Figure 19. Directionally solidified dendritic structure sectioned transverse to columnar grains. OM 50X

boundaries, are very irregular and serrated as seen in Figure 20. Grain boundary carbides are seen in Figure 21. The scanning electron micrograph in Figure 22 shows several important features. Most obvious are the large dark regions of coarse γ/γ' eutectic. The light colored particles are predominantly carbides (the thin long carbide is $\sim 100 \mu\text{m}$), and the grayish dendritic areas consist of fine γ/γ' .

4.2.2 Carbides

Carbides play an important role in the mechanical properties of Ni-base superalloys. The following figures illustrate the various morphologies found in the fir-tree specimens. Carbides of the MC-type, both blocky (Figure 23) and chinese-script (Figure 24) were very common. Small discrete carbides, which are generally characterized as $M_{23}C_6$ -type carbides, were also found in these specimens (Figure 25). The predominating carbide structure was the script-type. Script carbides can have the appearance of curved thin lines or straight lines, sometimes with very small particles which seem to be aligned on crystallographic planes. Script carbides have been known to have detrimental effects on fatigue (62). Analytical electron microscopy (AEM) performed on these carbides indicated that they are high in Ta, Ti, and Hf, while W and Mo were not concentrated in the script carbides. The AEM dot patterns are shown in Figure 26. Micropores were uncommon, but when found were usually associated with carbides near the γ/γ' eutectic regions. A micropore over

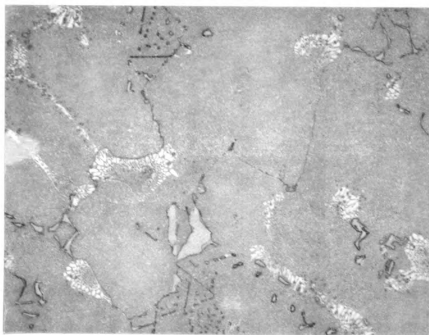


Figure 20. Serrated dendritic, or grain boundaries. OM 200X

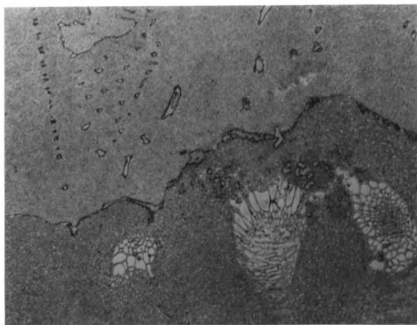


Figure 21. Grain boundary carbides. OM 400X

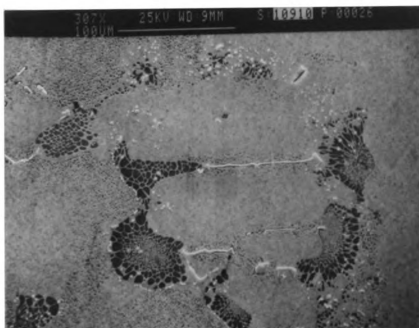


Figure 22. Microstructure showing large eutectic pools (dark), carbide particles (white) and dendritic areas of fine γ/γ' (grey). SEM 307X

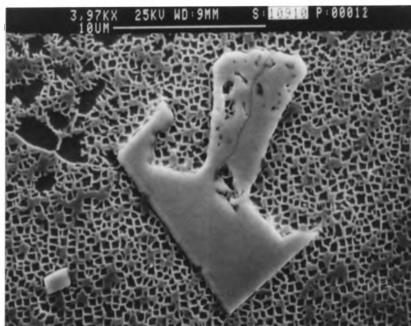


Figure 23. Blocky MC-type carbide. SEM 3,970X



Figure 24. Chinese-script (rosette) MC-type carbides. OM 400X

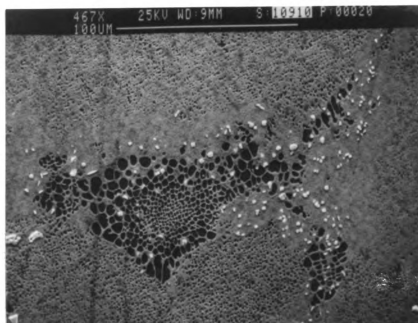
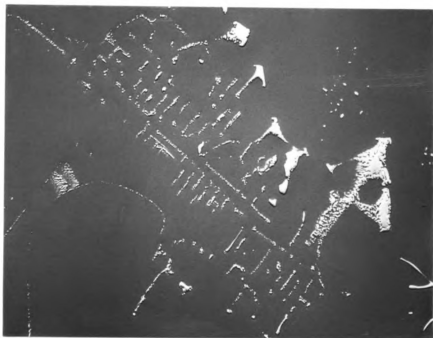


Figure 25. Small discrete M₂₃C₆-type carbides. SEM 467X

(a)



(b)

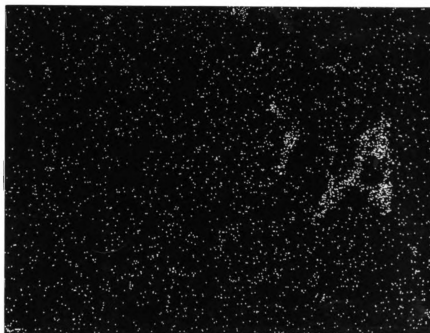
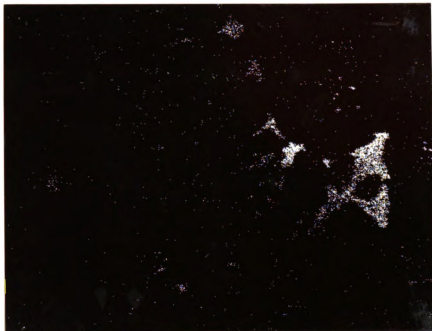


Figure 26. Analytical electron microscopy (AEM) dot patterns of script-type carbides, a. back scattered electrons, b. carbon, c. hafnium, d. tantalum, e. titanium, f. molybdenum and g. tungsten. AEM 400X

Figure 26 (cont'd.).

(c)



(d)

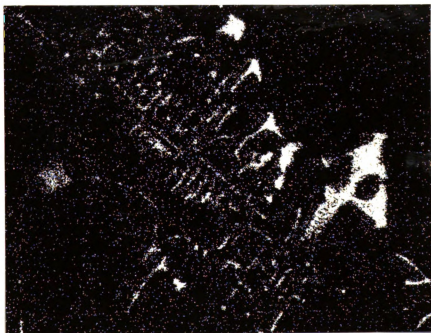
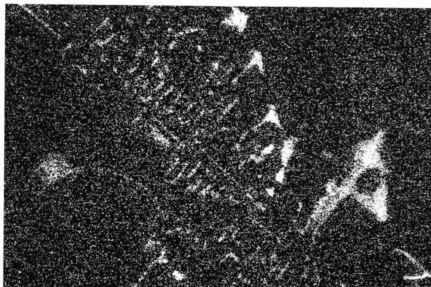
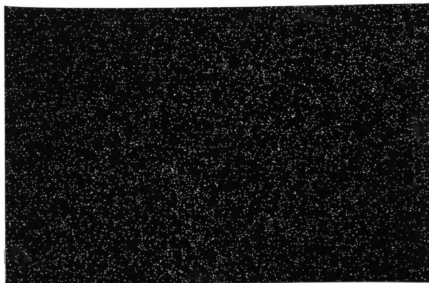


Figure 26 (cont'd.).

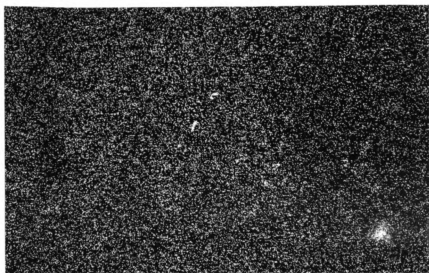
(e)



(f)



(g)



20 μm long is shown in Figure 27.

4.2.3 Gamma Prime (γ')

The volume fraction, V_v , of γ' in Mar-M 247 is reported to be approximately 62% (29). The γ' has a cubic morphology which is resolved in the SEM micrographs in Figures 23 and 27. This cubic morphology and its directionality is seen in the replica transmission electron micrograph in Figure 28. The average cube length in this micrograph is 0.5 μm . Gamma prime coarsening was believed to be noticed during SEM and TEM examination. This gamma prime coarsening is shown in the RTEM electron micrograph in Figure 29. Fine particles of randomly coarsened γ' are believed to be seen in the SEM micrograph of a carbide particle surrounded by a continuous layer of γ' (Figure 30). Precipitate coarsening will result in decreased fatigue resistance. As previously mentioned, this is due to the allowance of bypass deformation mechanisms with increasing interparticle distances associated with coarsening.

4.3 FIR-TREE REPLICAS

Analysis of the positive resin fir-tree attachment replicas taken from the fir-tree surfaces revealed several microstructural features on the surfaces of the specimens. Some of these features appear on one replica only, while other features



Figure 27. A micropore associated with a carbide. SEM 2,470X

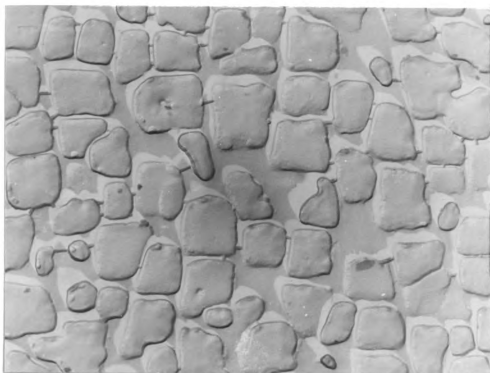


Figure 28. Cubic morphology and aligned directionality of gamma prime precipitates. RTM 19,000X



Figure 29. Gamma prime coarsening. RTEM 29,000X

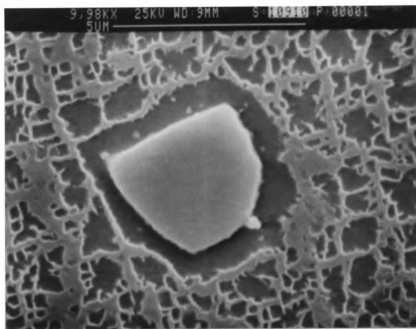


Figure 30. Carbide particle surrounded by a continuous layer of gamma prime (dark), and randomly coarsened gamma prime precipitates. SEM 9,980X

evolved during the continued fatigue cycling. The two-stage Reprosil dental impression medium/Spurr's low-viscosity resin replication technique was found to be excellent for tracing the development of, or alteration in, surface features. Two surface-changing features were prominent and both were found to affect the fatigue failures. These two "dynamic" features were the development of fretting wear and the development of oxide "polyps", a preferential oxidation process.

4.3.1 Fretting Wear

Fretting wear usually developed on the four contact regions of each fir-tree end. Occasionally wear would be noticed on both sides of one tang (only one side of a tang is considered to be a contact region). The evolution of the fretting wear was found to be consistent, with different stages of wear appearing during different fatigue cycles.

The following damage evolution was observed from examining the fir-tree replicas. The replicas taken at 0 cycles show slight surface roughness. The initial stages of fatigue testing resulted in adhesive wear which caused a large amount of damage and resulted in a very rough contact area. With continued testing the roughened surfaces slowly became smoothed down, except in a few localized regions where either debris accumulates or an excessive roughened area remained. After relatively long testing exposure (25,000 cycles), occasionally spherical

fretting particles formed. These spheres ususally developed in the areas of debris accumulation or localized roughening. These "spherical" particles are relatively large, approximately 0.1mm, often taking on an oval shape, but sometimes appearing perfectly spherical. With continued cycling, the material under the spherical debris becomes progressively damaged. Areas void of the spheres continue to become smoothened down or compacted, and develop parallel abrasive sliding wear grooves. The load bearing regions which have become smoothed down (but develop parallel abrasive wear grooves), macroscopically have a very shiny or polished appearance. It is believed that this shiny wear region has developed a compact oxide "glaze" as described by Wood et al (48). These replicas show the fretting wear and development of an oxide "glaze".

Throughout the entire fretting evolution, the contact area progressively increases in size as the wear region slowly extends into the non-fretted region. As this occurs, the fretted boundary, or the slip/no-slip boundary, continues to straighten out and becomes more pronounced.

Damage which occurs under the fretted spheres can be attributed to two interacting processes: physical wear and stress concentrations. The spherical debris causes physical wear which subsequently removes the surface protective oxide scale. The scale may be developed again and then removed. This action may cause the depletion of Cr and Al in the

underlying material, thus weakening the alloy. The spherical particles also become highly oxidized due to the high pressures and high localized temperatures which promote oxidation. These oxidized spheres may act to concentrate stresses under applied loads.

The different stages of the fretting wear development in the contact regions of the fir-tree specimens are illustrated in Figure 31. Generally, these stages were found to be:

1. Initial rough adhesive wear (Figure 31a).
2. Progressive smoothing of the initial damage, except in a few localised regions of excessive wear, or debris accumulation (Figure 31b).
3. The formation of spherical fretting particles in some of the areas of excessive wear or debris accumulation (Figure 31c) with associated underlying surface damage (Figure 31e).
4. Formation of an oxide "glaze". Formation characterized by a compacted or flattened region, with abrasive parallel sliding grooves and a very shiny surface (Figures 31d and 31e).

The excessive surface damage caused by a spherical fretting particle is shown in Figure 32. Three fretting spheres can be seen in the fretted regions in Figures 33 and 34. Most of the fretting spheres develop near the slip/no-slip boundary. As

(a)



(b)

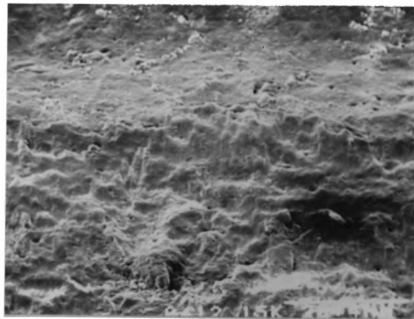
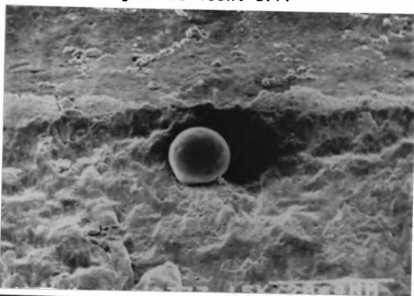


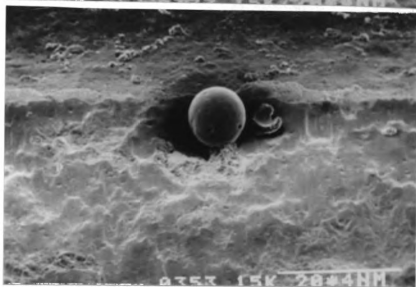
Figure 31. Different stages of fretting wear formed in contact regions. Specimen F109-14 Cr, RSEM 150X; a. initial rough adhesive wear (7,441 cycles), b. smoothing down of the initial damage (15K cycles), c. development of spherical fretting particles (25K cycles), note sphere formation is in region of excessive wear in a., d. retention of spherical particle and continued flattening of rouged area with associated "glaze" formation (30K cycles) and e. parallel abrasive grooves in glazed area and surface damage at fretting sphere location ($N_f=32K$).

Figure 31 (cont'd.).

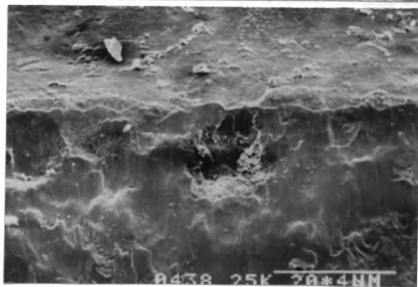
(c)



(d)



(e)



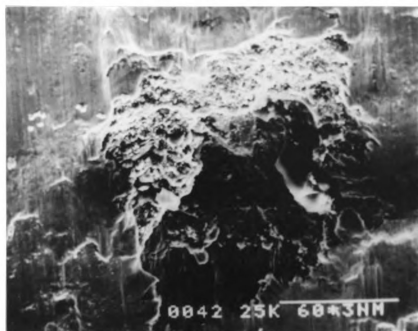


Figure 32. Excessive surface damage caused by a spherical fretting debris particle. SEM 500X

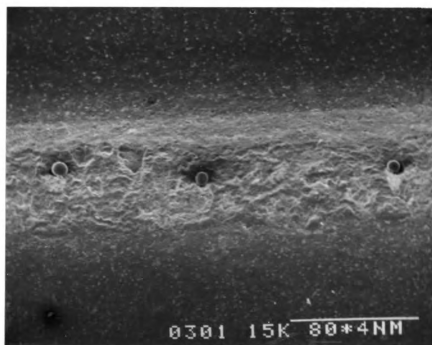


Figure 33. Three fretting spheres located in fretted region. RSEM 38X

(a)



(b)

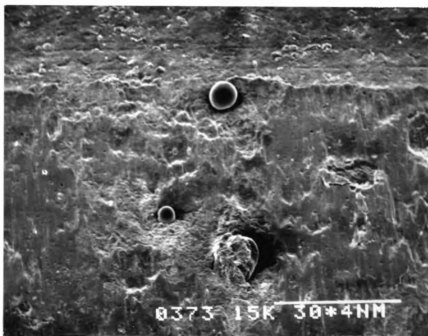


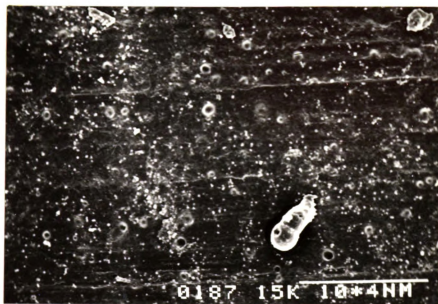
Figure 34. Spherical fretting debris; a. localized roughening at 15K cycles, b. sphere formation at roughened areas. RSEM 100X

mentioned, this is the region where stress and strain concentrations build up during fretting. Fretting spheres were found to develop only in the long life specimens. The earliest fretting spheres were found on replicas of F109-4 CR at 15,000 cycles. Although the spherical fretting particles damage the underlying material, and are believed to cause stress concentrations, the major form of damage from the fretting wear is believed to be due to the stress and strain concentrations which build up at the slip/no-slip boundary. It is near the fretted boundary that cracks which existed in the material were found to propagate to failure.

4.3.2 Preferential Oxidation

While examining the fir-tree attachment replicas, a second feature was found to develop with increasing fatigue cycles. Figure 35 depicts a series of electron micrographs which show this development or growth. The large surface feature (lower right area) is used as a reference point to clearly illustrate that these electron micrographs were taken of the same surface region. At the beginning of fatigue testing, the surface where these structures develop is either smooth or contains very small "white spots". As elevated temperature testing is conducted, bumps start to evolve in localized regions either at the small "white spots" or on smooth surface regions. These bumps increase in size with increased fatigue testing and develop with inherent cracks. It is believed, based on similar findings by

(a)



(b)

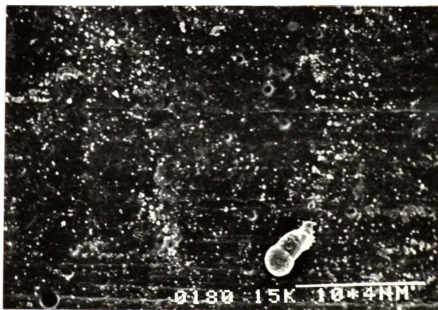


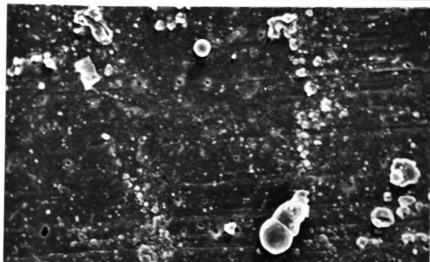
Figure 35. Development of oxide polyps. Specimen F109-1 F;
a. 0 cycles, b. 1587 cycles, c. 16,641 cycles,
d. 31,587 cycles and e. 46,587 cycles. RSEM 300X

Figure 35 (cont'd.).

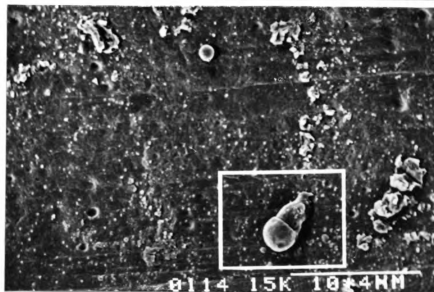
(c)



(d)



(e)



others (63), that these structures are some type of oxide polyp. Figure 36, of specimen F109-14 CR, some of these polyps with their inherent cracks are shown.

It was noticed on the replicas that the evolution of these oxides often take on a script morphology; as shown on the replica in Figure 37. The development of the polyps are the product of a preferential oxidation process involving carbides. This conclusion is based on the following: the polyps are inherently brittle and often arranged in script morphologies, they are similar to the particles Coffin (1) describes as "oxidized carbide particles which form polyps". These oxide polyps not only disrupt the surface layer, but their inherent cracks could be fatigue crack nucleation sites.

Replicas can be helpful in studying preferential oxidation growth rates such as these. The fastest development of these polyps was often in the initial stages of testing, with continued enlargement thereafter. The fir-tree replica examples in Appendix C, Figure 78, show the development of oxide polyps from a smooth surface to protruding features in a script morphology (lower center of micrographs).

4.3.3 Fatigue Cracks

Fatigue cracks were revealed from the replicas prior to the failure of three specimens. A long crack developed on specimen

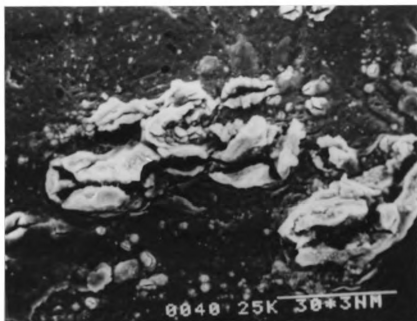


Figure 36. Oxide polyps with inherent cracks. SEM 1000X



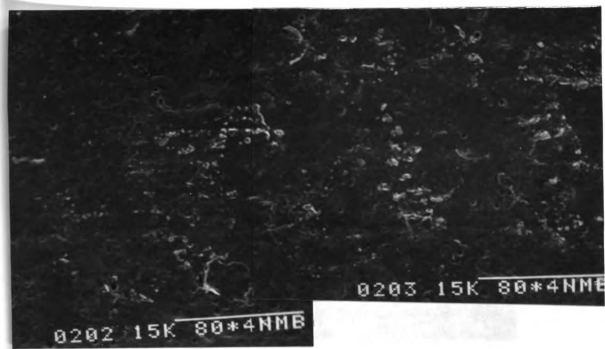
Figure 37. Oxide polyps with a script-morphology. RSEM 300X

F109-10 CR, in region A near the inner notch, between cycles 8,228 and 14,444. The specimen failed with the fracture initiating from this region with a fatigue life of N_f : 15,887, and with associated grip failure. Electron micrographs of this region show that the crack often propagates along paths of dense oxide polyp development. Figure 38 shows this crack region. A "branching" crack was observed to develop between cycles 31,587 and 46,587 on specimen F109-1 F, N_f : 51,309. This crack is shown on the 46,587 cycle replica (Figure 39) to exist along the fretted slip/no-slip boundary and is also extending down into the notched region. The fracture of this specimen did not initiate from the notched region, but from the crack branch along the slip/no-slip boundary. The replicas of specimen F109-4 CR revealed a crack which propagated between fatigue cycles 25,000 and 30,000 on the neck region of A₁. Electron micrographs of this regions are shown in Figure 78 in Appendix C. These were the only major cracks observed on the replicas. This replication technique could be used for crack growth data if the replicas are taken frequently enough.

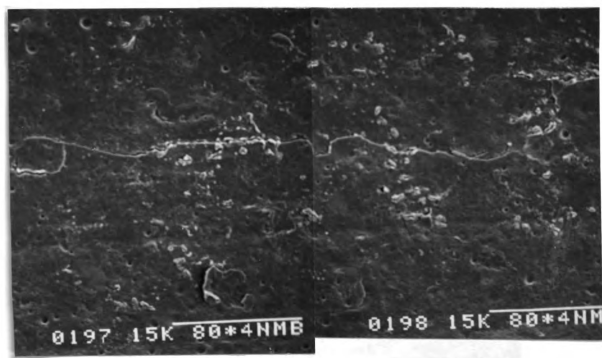
4.4 MACROSCOPIC EXAMINATION

4.4.1 Fretting Wear

Macroscopic examination of the fretted surfaces revealed the shiny, or polished, appearance of the wear regions. This



(a)



(b)

Figure 38. Crack of specimen F109-10 Cr; a. no evident of crack at 8,228 cycles and b. crack following dense path of polyps at 14,444 cycles. RSEM 190X



Figure 39. Crack of Specimen F109-1 F developed between cycles 31,587 and 46,587, this crack runs near the fretted slip/no-slip boundary and also extends into the notched region. RSEM 150X, 300X



was not evident with SEM examination. Shiny wear surfaces have smooth appearances but contain parallel abrasive grooves, where less shiny areas appear to be rough. In general, the outer contact regions are shinier and smoother than the inner contact regions. The excessive wear or gouged regions were noticeable macroscopically. Figure 40 is a macrograph of a localized gouged area within a shiny grooved fretted region. It appears that "glaze" formation, characterized by shiny surfaces with parallel abrasive grooves, only developed on load bearing surfaces which are subjected to excessive fretting wear. As mentioned, Wood et al (48) states that this "glaze" development may result from particles compacted together from the surfaces which may be thermally softened or even melted by the high localized temperatures attained in the load bearing regions. Once a thermally softened "glaze" layer is established a drop in friction and rate of wear is reported (48). In this study, it appears that with the development of the oxide glaze on the contact regions, further little wear occurred in those regions. Also, fatigue cracks did not propagate from within the regions of glaze formation.

4.4.2 Fractography

A "typical" fracture, one that does not involve a loading grip failure, initiates from an outer contact area either near the edge of the fretted wear, the slip/no-slip boundary. A side view showing a typical fracture surface can be seen in Figure

41. The directionally solidified dendritic structure can also be seen in this macrograph. Macroscopic examination of the fracture surfaces indicates there are several initiation sites with the microcracks coalescing into a macroscopic fatigue crack that propagates, thus producing the thumbnail region.

Three regions are distinguished on the fracture surfaces: a Stage I crack propagation region, a Stage II crack propagation region and a final fracture or overload region. Stage I is the initial propagation mode. Its macroscopic appearance is shiny and planar; and the crack region propagates obliquely to the stress axis. The color of the Stage I region is bronze on short life specimens, and silvery white on long life specimens. Stage II crack growth propagates normal to the stress axis. The Stage II crack is not shiny like Stage I, but some areas appear to be faceted. The Stage II area in short life specimens changes from bronze-yellow to light blue to dark blue at the edge of the thumbnail region. The Stage II area in long life specimens changes from silvery white, to light blue, to dark blue, to violet at the thumbnail edge. The final fracture, or overload region, has the same type of faceted appearance as Stage II, but it is more pronounced, and the fracture surface is randomly oriented with respect to the overload region. The final fracture area is uniformly brown with gold facets. The different colors of the three stages are associated with different oxide thicknesses which form during testing.

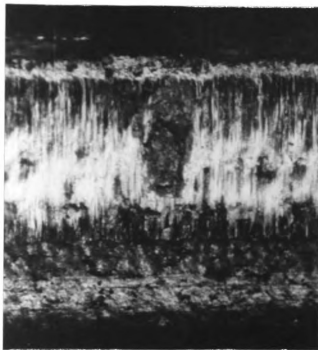


Figure 40. Macrograph of a localized gouged area within a shiny and grooved glazed fretted region.

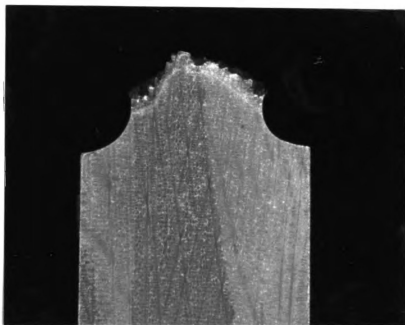


Figure 41. Side view of a "typical" fracture, the directionally solidified dendritic structure is visible. OM 6X

The fracture surfaces of the longest life specimen, F109-1 F (N_r: 51,309), and the shortest life specimen, F109-3 F (N_r: 11,531), are shown in Figures 42 and 43. Both failed under "typical" fracture conditions. The thumbnail fatigue crack propagation regions on these specimens are visible in these macrographs. The very bright region on F109-1 F indicates the region of extensive Stage I mode of crack propagation. The Stage I region on F109-3 F is much smaller. The thumbnail region of F109-1 F is smaller than that of F109-3 F, indicating a smaller stage II propagation region. As previously mentioned in the section on deformation, Stage I crack propagation modes in Ni-base superalloys are associated with planar heterogeneous slip (slip bands) on crystallographic planes, while stage II cracking is non-crystallographic, and due to homogeneous deformation (multiple slip) occurring normal to the stress axis. From fracture surface observations, it is concluded that directionally solidified Ni-base superalloys which exhibit an extensive Stage I fracture mode, with associated planar slip, have greater fatigue resistance than those with a short Stage I and extended Stage II mode of homogeneous crack propagation growth.

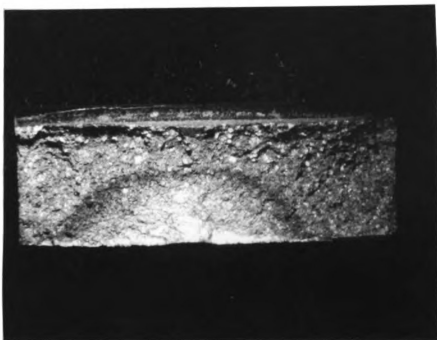


Figure 42. Fracture surface of the longest life specimen, F109-1 F, showing an extensive Stage I region (bright) in a thumbnail crack propagation region. OM 5X

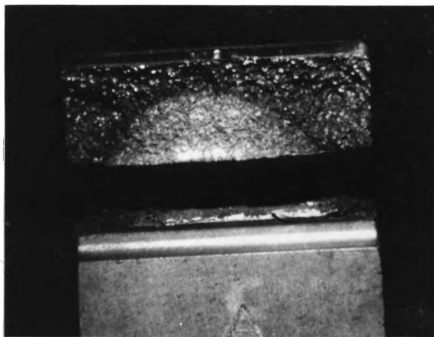


Figure 43. Fracture surface of the shortest life specimen, F109-3, displaying a shorter Stage I region. OM 4X

4.5 MICROSCOPIC EXAMINATION

4.5.1 Fractography

The following was observed from the fracture surface of four specimens (F109-3, -5, -10 and -1) which were examined with a scanning electron microscope. The Stage I fatigue crack propagation (FCP) has a distinctly smoother appearance on a microscopic level than the Stage II mode; which appears to propagate on various planes with an irregular appearance. The Stage II region was difficult to distinguish from the final fracture region. Secondary cracking was associated with both Stage II and final fracture regions. The extensive Stage I region of specimen F109-1 F can be seen in Figure 44. The smoothness, or planarity of Stage I is shown in Figure 45. Suspected intersecting slip steps in the Stage I crack region of specimens F109-1 F and F109-3 F are shown in Figures 46 and 47 respectively. The final fracture region of F109-3 F is shown in Figure 48. This is a typical example of the overload region which is characterized by a rough, almost dimple-like, surface and secondary cracking.

As previously mentioned, parts of the overload and Stage II fracture surfaces appear faceted when viewed macroscopically. Microscopically these areas are planar and seem to have a crystallographic appearance. These areas usually display straight and perpendicularly intersecting "lines" in the

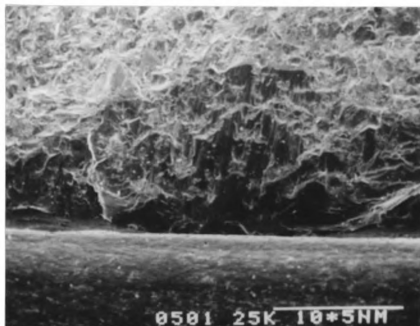


Figure 44. Micrograph of the extensive Stage I region of specimen F109-1 (extending approximately 15mm). SEM 30X

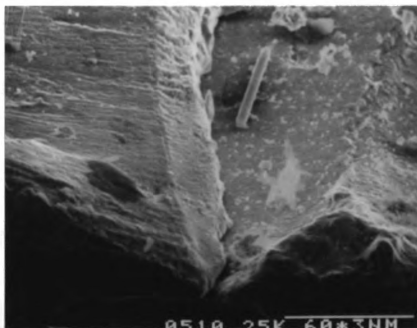


Figure 45. The smoothness or planarity of Stage I crack propagation is seen in this micrograph where two planes of crack growth intersect. SEM 500X

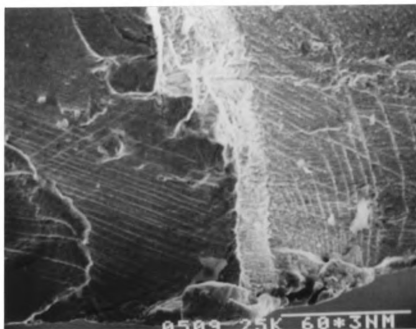


Figure 46. Intersecting slip steps in Stage I crack growth region. SEM 500X

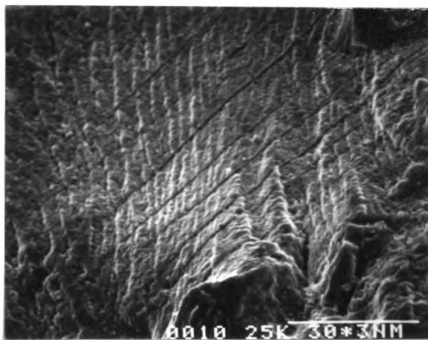


Figure 47. Intersecting slip steps on the order of 10 microns in Stage I crack growth region. SEM 1000X

otherwise non-crystallographic, non-planar fracture surface. One of these planar regions stands out in the rough overload fracture surface of specimen F109-10 CR in Figure 49. A higher magnification view of one of these planar regions is shown in Figure 50. Particles or inclusions can be seen on these planar surfaces. Often the distribution of these particles were found to take on a script morphology similar to those in Figure 51. The particles associated with these regions are believed to be carbides and the planar surfaces in the non-planar fracture regions are believed to be the result of a change in deformation mode and crack propagation rate at these carbide particles. This is best illustrated in Figure 52 where the Stage I planar crack propagation mode is abruptly changed at a script carbide. Carbide alignment orientation has been reported by Gemma et al (64) to be responsible for variations in the crack growth rates in a DS Ni-base superalloy. It is believed that script carbides are detrimental to fatigue resistance by changing the fatigue crack propagation mode and thus increasing the crack growth rate.

4.5.2 Crack Nucleation

Scanning electron microscopy studies of surfaces in the fracture vicinity provided information on fatigue crack nucleation sites. Figure 53 is a low magnification electron micrograph which shows the propagation of the fracture crack to be near the slip/no-slip boundary. A closer examination of this

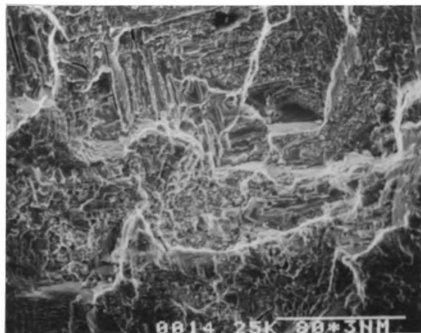


Figure 48. Final fracture region characterized by a rough almost dimple-like surface and secondary cracking. SEM 380X

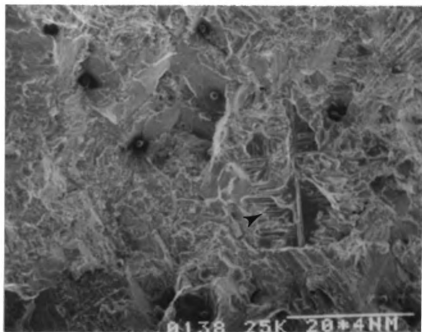


Figure 49. A faceted, planar fracture region (middle right) with perpendicularly intersecting lines in rough overload, non-planar region. SEM 150X

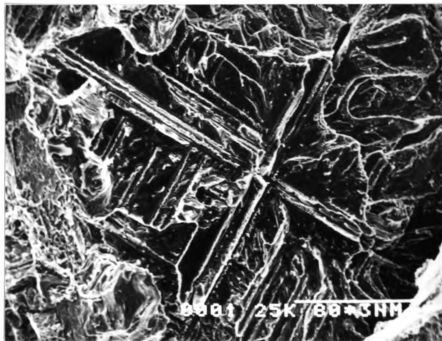


Figure 50. Faceted fracture region with intersecting perpendicular lines in final fracture region. SEM 380X

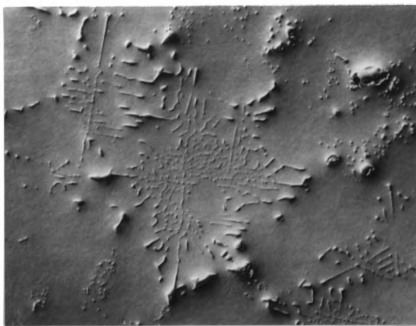


Figure 51. Carbides with script-type morphologies illustrating perpendicularly intersecting lines and other shapes found on faceted fractured surfaces. OM 200X

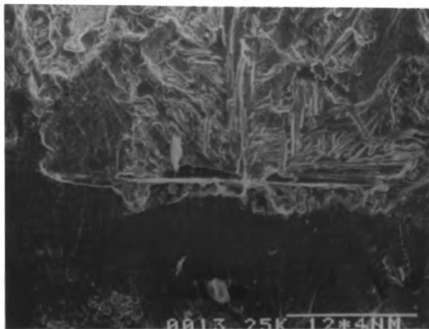


Figure 52. The smooth Stage I mode of crack propagation is abruptly changed at a script carbide. The drawing distinguishes the carbide particles which have been darkened. SEM 250X

region reveals that the macrocrack (fatigue crack) had several initiation sites. These individual sites are believed to be from oxide polyps; one of these is shown in Figure 54. Figure 55 shows another interesting influence of these polyps. A deep oxide polyp area caused the plane of fracture to separate.

The nucleation of a fatigue crack from an oxide polyp is shown in Figure 56. Nucleation of fatigue cracks from polyps usually occurs near the slip/no-slip boundary where the stresses are highest, as shown in Figure 57. Figure 58 shows a group of oxide polyps initiating fatigue cracks near the fretted boundary. An interesting observation about this electron micrograph is the propagation of a crack to the fretted boundary, with the surface wear extending over the crack. This indicates that as the contact region increases in size, polyp cracks may lie underneath the fretted region, resulting in even higher stress concentrations near the fretted boundary. Figure 59 shows the opening up of a fracture region which initiated from an oxide polyp at the fretted boundary. The inherent brittleness of the polyp is illustrated by the secondary cracking associated with this oxide on the fractured surface. These oxidized carbide polyps are found to be detrimental to fatigue resistance. The polyps disrupt the protective oxide layer, while the inherent cracks are believed to mechanically and chemically weaken the material, resulting in the nucleation fatigue cracks.

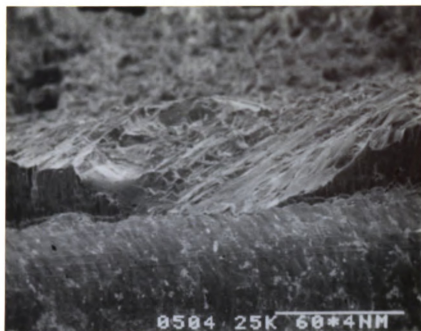


Figure 53. Propagation of the fracture crack from the slip/no-slip fretted boundary. SEM 50X

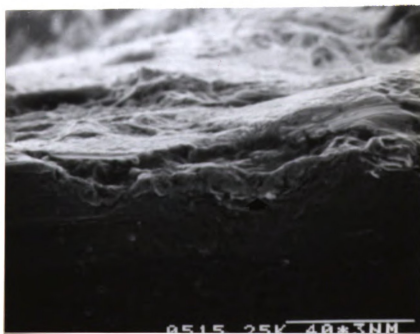


Figure 54. Initiation site of a fatigue crack at an oxide polyp. SEM 750X

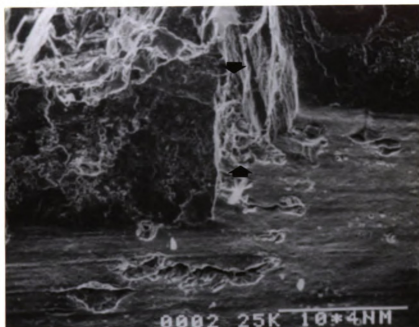


Figure 55. A deep oxide polyp area caused the plane of fracture to separate. SEM 300X

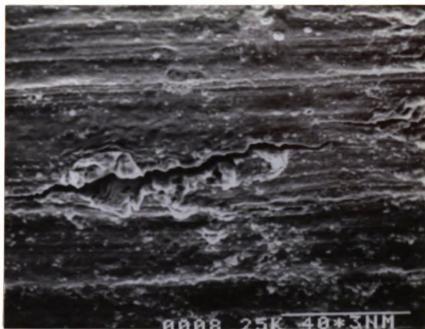


Figure 56. Nucleation of a fatigue crack from an oxide polyp. SEM 750X

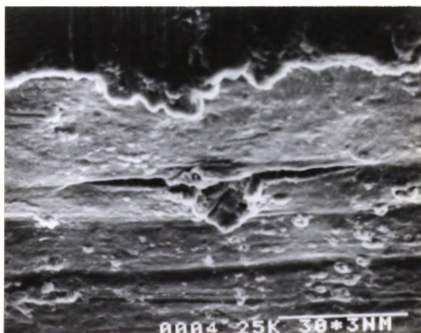


Figure 57. Nucleation of a fatigue crack from an oxide polyp near the slip/no-slip fretted boundary (upper section of picture). SEM 1000X

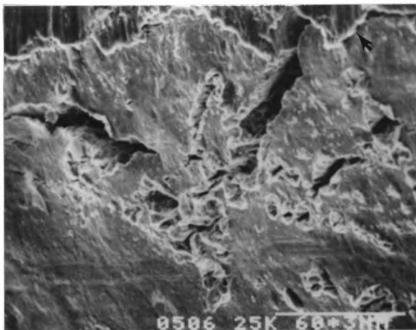


Figure 58. A group of oxide polyps initiating fatigue cracks near the fretted boundary, note the wear region extending over the crack in the upper right corner. SEM 500X

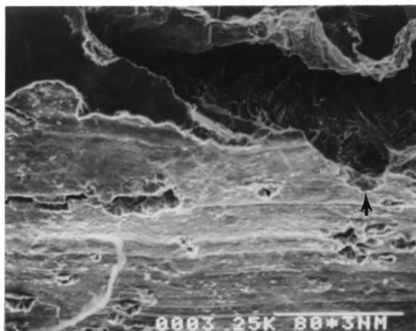


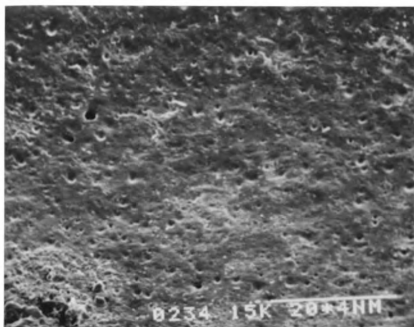
Figure 59. Opening up of a fracture region at an oxide polyp at the fretted slip/no-slip boundary (right side). The brittleness of the polyp is illustrated by the secondary cracking. SEM 380X

4.6 INCIPIENT MELTING

Incipient melting was observed on the surface of a few specimens and a few replicas. The replicas of specimen F109-10 CR show the introduction of splashed spheres between the cycles 1,500 and 8,228 (Figure 60). These spheres are similar to the one shown in Figure 61 of specimen F109-5 F. Other areas of incipient melting on F109-5 F are shown in Figure 62 and 63. Figure 63 also shows fatigue cracking at oxide polyps. Wood (48) and Engel and Klingele (49) both discuss the possibility of incipient melting resulting from sliding wear. This is attributed to the high localized pressures and temperatures. The spherical particle in Figure 64 is sitting just inside the boundary of the wear region where localized melting has occurred and recorded the cyclic movement in the smooth melted region. Incipient melting of this type indicate that the contact pressures and resulting localized temperatures may be higher than expected under these conditions; with incipient melting and its associated detrimental effects possible under similar conditions in turbine engines.

The crack that resulted in the fracture of grip #6 initiated from a very large surface discontinuity. Specimen F109-14 CR which was in the loading grip at the time of the failure, had a similar discontinuity located adjacent to the one on the grip (specimen location: \underline{B}_{1N}). These large surface defects have an appearance which is characteristic of an area

(a)



(b)

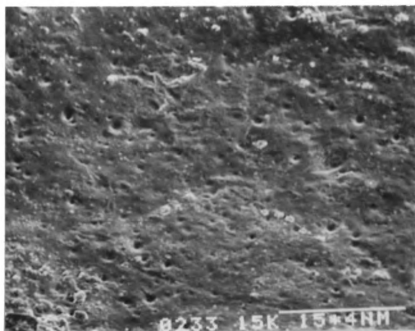
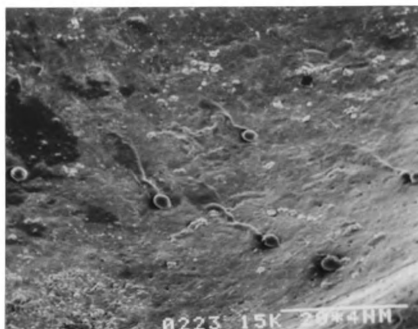


Figure 60. Replicas of specimen F109-10 Cr showing the introduction of splashed spheres; a. 0 cycles, b. 1,500 cycles, c. 8,228 cycles and d. 14,444 cycles. RSEM 150X

Figure 60 (cont'd.).

(c)



(d)

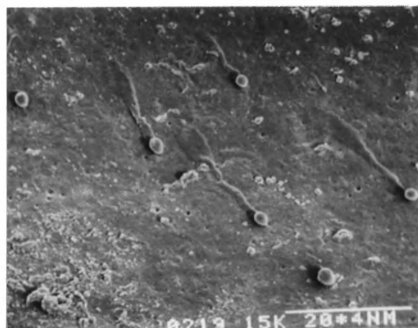




Figure 61. Incipient melting splashed sphere on F109-5 F, similar to those in figure 60. SEM 1000X



Figure 62. Dripping sphere: incipient melting area characterized by glassy, very smooth appearance. SEM 500X

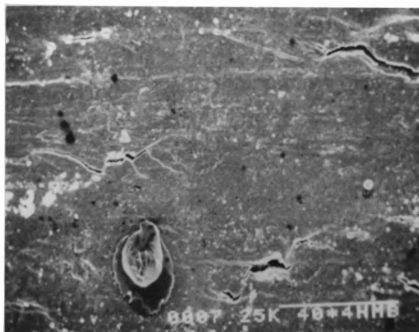


Figure 63. Evidence of incipient melting (feature in lower left area). Cracking at oxide polyps. SEM 375X



Figure 64. A spherical particle located just inside the boundary of the wear region where localized melting has occurred and recorded the cyclic movement in the smooth melted region. SEM 1500X

being melted and then quickly re-solidified, including: rounded markings, melt craters, quenched droplets from splashing of molten metal and solidification shrinkage cracks. The surface discontinuity with associated melt droplets and rapid solidification cracks on the specimen are shown in Figures 65, 66 and 67. Melted zones such as these have mechanical notch effects along with metallurgical effects. Shrinkage and transformation stresses are produced in the material resulting in favored sites for the initiation of fatigue cracks under conditions of alternating loads (49). Specimen F109-14 CR had a similar discontinuity on tang A_{OUT}. The SEM replicas indicate that both of these surface defects appear between 25,000 cycles and 30,000 cycles. The test stopped with the grip failing at 32,564 cycles. Engel and Klingele (49) report that localized heating and melting of metal surfaces often results from the undesired transmission of electrical current. It is possible that these surface discontinuities could have resulted from undesired electrical current transfer, occurring perhaps during spot welding of the thermocouples to the specimens center.

A very similar type of surface feature as the one found on F109-14 CR region B_{IN}, was also found on specimen, F109-1 F, Figure 68. The location was out of the fir-tree area, but within the gripping area. Since this type of defect results in very fine features, some seemingly dendritic in nature, this area was used to evaluate the replication quality and is shown in Figures 75, 76 and 77 in Appendix C.

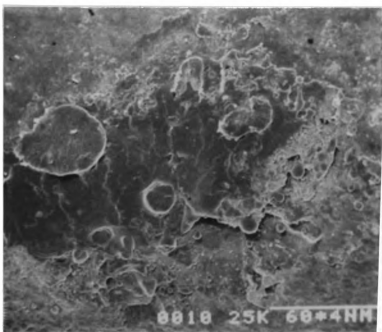


Figure 65. Replica of large surface discontinuity on specimen F109-14 Cr having characteristics of melting and rapidly solidifying; melt droplets, melt craters and solidification shrinkage cracks. RSEM 50X

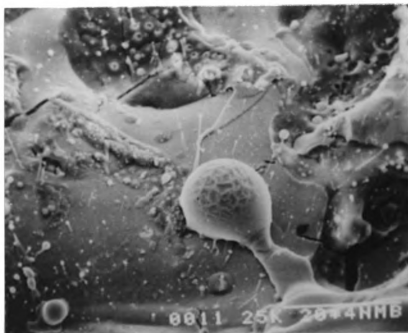


Figure 66. Higher magnification of Figure 65 showing quenched droplets from splashing of molten metal and rapid solidification cracks. RSEM 750X



Figure 67. Splashed quenched droplets radiating away from the large surface discontinuity in Figure 65. SEM 150X

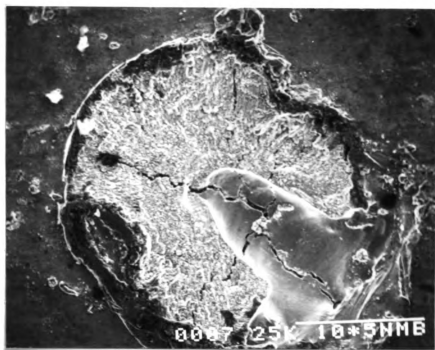


Figure 68. Large surface discontinuity on Specimen F109-1 F. SEM 150X

CHAPTER 5

CONCLUSIONS

No direct conclusions can be made between the effect of the specimen geometries (flat versus crowned) and the fatigue lives. A flat specimen, F109-1 F, had the longest life with N_f : 51,309. The specimen with the second longest fatigue life had a crowned geometry, F109-4 CR, with N_f : 47,302, but it also had an associated loading grip fracture. The three shortest life specimens all failed from the same side of the A fir-tree end, and were all loaded into grip #3. The interaction between the grips and the specimens played an important factor in the fatigue life. Geometry alone does not allow for increases in fatigue life. This amplifies the importance of the contact conditions (materials, temperatures, environment, oscillatory frequency, coefficient of friction, wear mechanisms, etc. in addition to stress distributions) in fretting situations.

The replication technique, Reprosil elastomeric impression medium/Spurr's low-viscosity resin, was found to be an excellent technique for applications on large and curved surfaces such as the fir-tree attachment ends. The Reprosil/Spurr's resin combination had good reproductive quality up to high magnifications

and could replicate spherical particles and protruding features. These replicas do not warp upon replicating curved surfaces like the common replicating technique involving cellulose acetate replicating tape.

Scanning electron microscopy examination of the fir-tree replicas revealed two prominent surface-changing features which were associated with the fatigue failures. These two "dynamic" features included the development of fretting wear and preferential oxidation of carbides. Both of these features were found to affect fracture initiation.

Fretting wear was observed at the load bearing, or contact surfaces, of the fir-tree specimens. The following models the sequence of fretting wear occurring on the load bearing surfaces during fatigue testing, as concluded from the replicas:

1. Initial rough adhesive wear.
2. Progressive smoothing of the initial damage, except in a few localized regions of excessive wear or debris accumulation.
3. The formation of large ($\sim 0.1\text{mm}$) spherical fretting particles in some of the areas of excessive wear or debris accumulation, with associated underlying damage.
4. Formation of an oxide "glaze", characterized by a compacted or flattened region with abrasive sliding grooves and a very shiny surface.

The spherical debris particles, which only formed in the long life specimens, were found to increase in size and cause surface damage. The spherical particles are believed to be highly oxidized and hard, and resulted in local stress concentrations. The detrimental effect of the fretting wear was found to be the build up of stresses and strains at the fretting boundary, or the slip/no-slip boundary. It is from this region where fatigue cracks often propagated from.

The second "dynamic" feature revealed by the replicas was the evolution of oxide polyps on the surface of the specimens. Elevated-temperature fatigue testing caused polyps to develop and grow with increasing fatigue cycles. The polyps were shown to nucleate from either very small bumps or smooth areas. These oxide polyps are brittle and evolve with inherent cracks. The polyps take on a script morphology and are believed to be the result of preferential oxidation of carbides. These oxide polyps nucleate fatigue cracks, especially near the fretted slip/no-slip boundary.

Once a fatigue crack starts to propagate, fretting wear has little further influence on the fatigue life. The fatigue cracks in these specimens propagated transgranularly and fractography revealed three different fracture regions. Two fatigue crack propagation (Stage I and Stage II) regions made up a thumbnail fracture area. The third region being the final fracture or overload region. The initial, Stage I mode of crack

growth, propagated oblique to the stress axis and was characterized by a planar and smooth fracture appearance. In the stage II mode, the crack propagated normal to the stress axis and was characterized by non-planar rough fracture surface. The final fracture (overload) region was similar in appearance to the Stage II mode, but the propagation was random with respect to the stress axis. Stage I is associated with heterogeneous planar deformation structures and Stage II with homogeneous deformation structures. Gamma prime coarsening, which was found in these specimens, encourages Stage II crack propagation. Script-type carbides were found to change the crack propagation mode. It is thought that the script carbides alter the crack growth rate in a detrimental manner. Specimens with extensive Stage I fatigue crack propagation regions were found to exhibit longer lives than specimens with short Stage I crack growth and extensive Stage II crack growth.

These specimens failed by fretting fatigue which was greatly influenced by the contact conditions. Fatigue cracks nucleated at oxide polyyps and the final fractures propagated from cracked polyyps near the fretted slip/no-slip boundary.

APPENDICES

APPENDIX A

METALLOGRAPHY PREPARATION

Metallography specimens (optical, scanning electron and analytical electron) were prepared using standard techniques. Specimens were mounted in bakelite and rough polished using silicon carbide papers in the grit sequence of 240, 320, 400 and 600. Polishing was continued using diamond pastes of 6 micron and 1 micron; final polishing was done using 0.05 micron alumina slurry. Specimens were either examined in the unetched condition or were etched using a solution of 33% nitric acid, 33% acetic acid, 33% water and 1% hydrofluoric acid with immersion times of 10-20 seconds.

APPENDIX B

TEM REPLICAS

Transmission electron microscope replicas (RTEM) were taken from the fatigue tested specimen F109-10 Cr, N,=15,887, on a polished and etched (see Appendix A) section normal to the applied stress.

The following materials and procedures were used to make the negative replicas.

B.1 MATERIALS

Cellulose acetate replicating tape

Acetone

Pipette

Small glass dish

Copper grids (300 & 400 mesh)

Carbon and platinum evaporants

Filter paper, razors, tape, glass slide

Cleaned, polished and etched sample

B.2 PROCEDURES

1. Uniformly wet the specimen surface with a thin layer of acetone.
2. Put a strip of cellulose acetate (replicating tape) onto the specimen surface and apply slight pressure to ensure proper relief.
3. After the cellulose acetate has completely dried, carefully remove it from the specimen surface. Dispose of the first replica, which cleans the surface of debris, unless artifacts are important. Repeat steps 1, 2 and 3 until an intact replica is made.
4. Tape the replica upright onto a glass slide and label orientations.
5. Place the glass slide and replica into a vacuum evaporator and evaporate a medium layer of carbon directly onto the replica. Then evaporate a layer of chromium (or Pt, Au, etc.) onto the replica at a known angle (30 degree).
6. Remove the coated replica and dissolve the cellulose acetate negative with acetone:
 - A. Cut 2 mm to 3 mm squares from the replica with razor

blades. Set these on the Cu-grids and place them on the filter paper in the glass dish.

B. Wet the filter paper with acetone and be sure not to drop acetone directly on the replicas.

C. Keep the paper wet with acetone and periodically move the grids to new positions.

D. Be sure ALL of the acetate is dissolved; this will take approximately one hour.

7. Place Cu-grids containing the carbon-chromium replicas into the TEM and examine.

Supplementary reading:

Goodhew, P. J. "Specimen Preparation in Materials Science", in Practical Methods in Electron Microscopy. Vol. 1, Part 1, Chpt 5. A. M. Glauert, ed. North-Holland Pub. Co., 1983.

Ladd, M. W. The Electron Microscopy Handbook. Ladd Research Industris, 1973, pp. 18-30.

APPENDIX C

FIR-TREE REPLICAS: PROCEDURES AND EVALUATION

The following describes the two-stage replication technique which was used to replicate the specimens fir-tree attachment surfaces. This replication technique involves making negative replicas with Reprosil elastomer impression material. Positive replicas are then made from the negative replica molds using Spurr's low-viscosity resin. It is believed that this is the first application of this technique to materials science.

C.1 MATERIALS

Reprosil Light Body Vinyl Polysiloxane Impression Material

(manufactured by the L. D. Caulk Co.). Available from most dental supply companies.

Spurr's Epoxy Resin (ERL), a low-viscosity resin which can be purchased in kit form.

Spatula

Airbrush or Freon Duster

Gold evaporant

Container designed to support repositil around specimen surface of interest (if necessary)

C.2 PROCEDURES

C.2.1 Preparation for Making Positive Replicas

Mix the Spurr's low-viscosity resin to give the "firm" hardness.

Table 3. Resin Components

<u>COMPONENT (gr or ml)</u>	<u>B(Firm)</u>
ERL-4206 (Vinyl Cyclohexene Dioxide)	10.0
DER 736 (Diglycidyl Ether of Propylene Glycol)	6.0
NSA (Nonenyl Succinic Anhydride)	26.0
<u>S-1 (DMAE, Dimethylaminoethanol)</u>	<u>0.4</u>

- A. Carefully handling these chemicals (gloves), measure and mix them together under a vented hood. These chemicals are carcinogenic.
- B. Refrigerate the mixed resin over night (before use). Can be stored covered in refrigerator several days.
- C. After refrigeration, bring the resin to room temperature before use and do not stir.

C.2.2 Preparation for Making Negative Replicas

Analyze the specimen surface to be replicated and determine if a restraining container will be necessary to support the reposit (negative replicating material) around the specimen's area of interest while it cures (hardens). The following relates to the fir-tree attachment specimens.

1. Due to the specimen curvature and the desire to replicate large surface areas, a quartz container was designed* and built in which one entire fir-tree attachment end of a specimen could be replicated (figure 69). *Major J. Marksteiner

2. The quartz container was designed with flat sides so that the negative replica would have a flat bottom to support itself during the pouring and curing of the resin (positive replica).

3. The quartz container was built to be easily disassembled (figure 71) so the hardened replica could be easily removed without damage of tearing.

4. The use of a restraining container to support the Reposit has the advantage of producing reliable, uniformly sized replicas which aid in the handling and analyzing of the final replicas.

5. Quartz was a good material to make the container from

because the glassy surface finish prevents the replicating medium from sticking to it, and it is transparent so that errors and pores are noticeable.

C.2.3 Making Negative Replicas

1. Measure equal amounts of the Reprosil base (orange) and catalyst (white), mix rapidly and thoroughly for about 45 seconds until the mixture is streak-free.
2. Apply a thin uniform layer of the Reprosil mixture onto the surface(s) of interest. With an air brush (or freon duster) apply moderate pressure onto the mixture to ensure direct contact with all surface features and elimination of all air bubbles.
3. Apply a thick layer of Reprosil onto the bubble-free thin layer, too much is better than too little. If a restraining container is used, fill it with the reprotsil mixture as well, place covered specimen inside. Be sure to leave adequate room between all surfaces of the specimen and the container when used. It is necessary that a thick layer of replicating medium is allowed to form all around the specimen's area of interest. (A large paper clip was used to support the fir-tree specimens in the quartz container at a known depth, figure 69).

4. Let the Reprosil cure (harden) completely. This will take about 5-8 minutes at room temperature. Carefully remove the Reprosil replica from the specimen and label. (For the fir-tree specimens the quartz container was disassembled and the replica and specimen removed together as a unit. The replica was then carefully cut in half and peeled from the specimen). These replicas are very flexible and recover their hardened shape but they can tear easily if made too thin.

5. If a container was not used then trim the back of the replica so that it is flat.

6. Using a small amount of Reprosil mixture make a slight ridge around the edge of the replica and let cure. This will support the low viscosity resin when making the positive replica. Take care not to drip Reprosil on the area of interest when making the ridge. (The fir-tree Reprosil replicas were cut in half, removed from the specimen and then "glued" together with additional reprosil mixture to make a single negative replica mold of one entire end of a fir-tree specimen, figure 72).

7. After replicas are hardened they are ready to be used as molds for the positive replicas. It is recommended that positive replicas be made within about a week of making the negative replicas, as these reprosil replicas can "relax" after a few days and the replicating accuracy will decrease with time.

8. The negative replicas can be plated with a thin layer of metal (Au or Pt) and directly examined with a SEM. This technique can be confusing since the inverse image will be presented, also low accelerating voltages must be used (<20KV) as the electron beam can damage (melt) the reposit, contaminating the SEM column as well.

C.2.4 Making Positive Replicas

Cured Reposit (negative) replicas are dimensionally stable for several days before they begin to loose and detail; a group of resin replicas can be cured at once.

1. Bring the refrigerated Spurr's Epoxy Resin to room temperature before using. DO NOT remix or stir the resin, this will introduce many fine air bubbles and ruin the replicas.

2. Carefully and slowly pour the resin into the negative reposit replica molds, fill to top of ridge. If air bubbles develop against the Reposit carefully try to remove them. Centrifugal casting is ideal, but not necessary.

3. Place the resin filled negative molds into a 60-70°C oven for 6 to 12 hours to cure. Be sure that the resin is hard. If the resin is not hard, it has not cured correctly and should be discarded. The fir-tree specimens were cured under 150W, 120V

flood lamps, at a predetermined distance to provide ~60°C, under a vented hood for 6-10 hours.

4. After resin replicas are cured (hard) and cooled, carefully peel off the Reprosil replica, label specimens and store. The resin replicas are now very brittle and can easily fracture.

C.2.5 Preparation for SEM Examination

1. Sputter or evaporate a thin layer of gold (or Pt) onto the replicas. Vacuum evaporation may not produce a uniform layer, especially on curved surfaces, so if a rotary evaporator is not available the replicas should be moved to be evaporated from different angles and directions. Sputter-coating can produce a more uniform layer, even on certain curved surfaces but can melt or deform the replicas if they are not properly cured, or if they become too hot. Sputter-coating can take from 5-10 minutes whereas vacuum evaporation can take from 1.5 to 2.5 hours. Charging will occur upon SEM examination on specimens which are not properly coated. Coating with too thick a layer of metal can cover details.

2. Mount the coated replicas on a SEM stub and secure with electrically conductive paint (silver or TV tube carbon). Paint a conductive line from the coated surface to the stub. Be careful not to paint the areas of interest. Allow adequate time

for complete drying of conductive paints.

3. Analyze the coated replicas at or below 15KV (20KV max.).

Above this accelerating voltage damage can occur to the replica resulting in SEM column contamination.

Figures 69-72 show the sequence of making the Reprosil/Spurr's resin fir-tree replicas. The sequence is summarized as follows: 1. design a constraining container to support the Reprosil medium, Figure 69, 2. mix and apply the Reprosil to the fir-tree surfaces, Figure 70, 3. cure and remove the negative Reprosil replica, Figure 71, make a mold out of negative replica, pour and cure the premade Spurr's resin, remove the hardened positive resin replica, and finally, coat with gold for SEM examination, Figure 72.

C.3 EVALUATION OF THE REPLICATION TECHNIQUE

1. The Reprosil/Spurr's Epoxy Resin replicas are an excellent technique for replicating curved surfaces. Cellulose acetate replicas (commonly used) tends to warp when used for replicating curved (or notched) areas; the Reprosil/Spurr's resin replicas do not warp.

2. The Reprosil/Spurr's resin replicas are excellent for large and hard to reach surfaces.



Figure 69. Fir-tree specimen, supported by large paper clip, centered in quartz constraining container. Note adequate air space surrounds specimen to allow for a uniform, thick layer of Reprosil. 0.8X

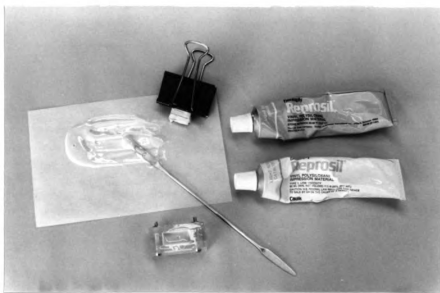


Figure 70. A thin streak-free, bubble-free, layer of Reprosil catalyst and base (50/50) is applied to the specimen surface. The container is then filled and the specimen set inside.

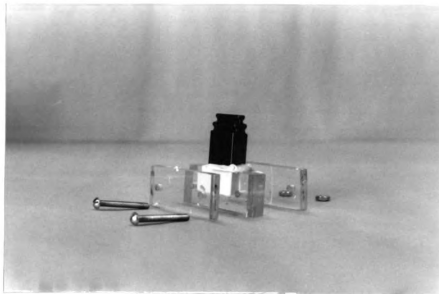


Figure 71. After the Reprosil is hardened, the quartz container is disassembled for easy, non-damaging removal of both the specimen and the replica together.

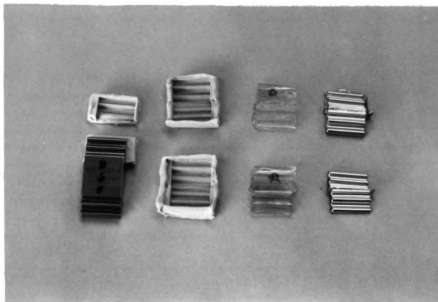


Figure 72. Replica steps, from left to right; a. the Reprosil negative replica is cut in half and trimmed, b. the two halves are "glued" together and a ridge is made around the top edge with additional Reprosil, c. the Spurr's resin is poured and cured in the negative replica mold (the positive permanent replica), and d. the positive resin replica is coated with gold.

3. This technique is excellent for replicating and tracing topographical detail such as fretted regions, Figure 73. Spherical and protruding particles can also be replicated, Figure 74. The Reprosil allows for forming around particles with easy, flexible removal; unlike the brittle cellulose acetate.

4. The quality of the replicas was found to be very good. Figures 75, 76 and 77 compare replicas and the corresponding specimen areas at magnifications of 500X, 1000X (1250X) and 2500X. The replicas are examined at 15 KV accelerating voltage while the specimens are examined at 25KV. When comparing the replicas to the specimen it should be remembered that higher accelerating voltages yield better resolution. These specimens were coated with a relatively thick layer of gold. If a thinner layer of gold was applied, better reproductive quality could be attained.

5. The Reprosil elastomeric impression medium is dimensionally stable for several days, several positive replicas can be cured together. The positive resin replicas will not lose and maintain dimensional stability when properly cured, and so are permanent replicas.

6. A few of the positive resin replicas exhibited very porous surfaces. This is attributed to one or more of the following replicating errors, which need to be avoided.

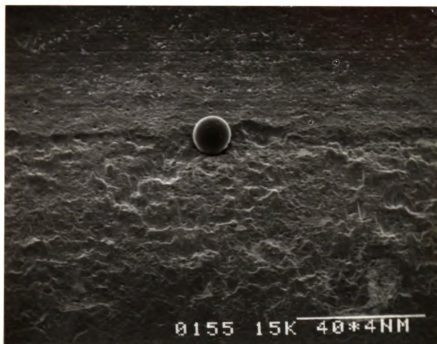
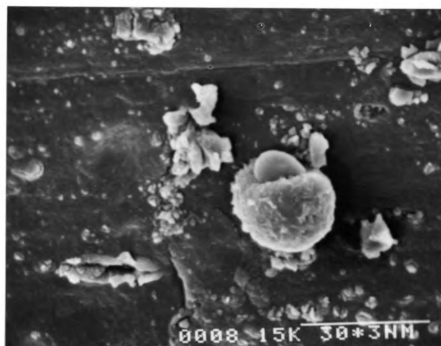


Figure 73. Replica of a fretting sphere near the fretted boundary of specimen F109-1 F taken at 31,587 cycles. RSEM 75X

(a)



(b)

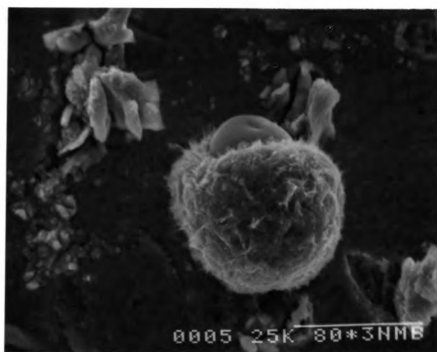


Figure 74. Replication of spherical and protruding features:
a. replica at 46,587 cycles, 1000X, b. specimen
with $N_s=51,309$. 1900X

(a)

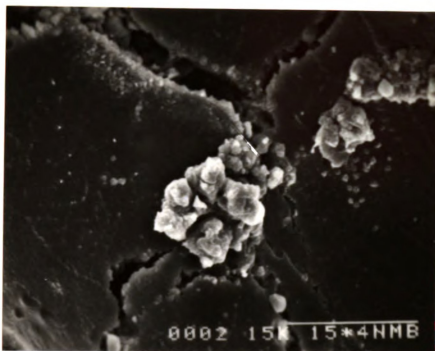


(b)



Figure 75. Direct comparison of replica and corresponding specimen area: a. specimen 500X (25KV) and b. replica 500X (15KV).

(a)



(b)

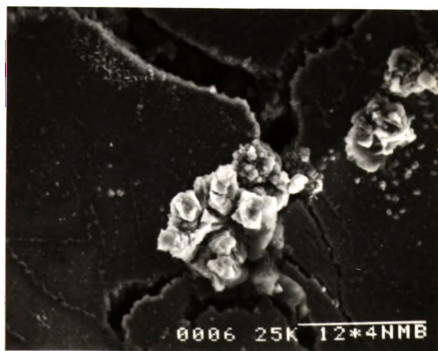
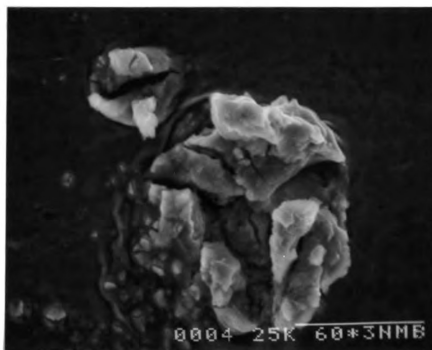


Figure 76. Replica quality comparison: a. replica 1000X (15KV) and b. specimen 1250X (25KV).

(a)



(b)

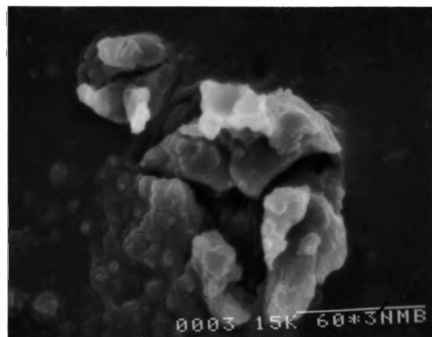


Figure 77. Replica loses some detail at higher magnification: a. specimen 2500X (25KV) and b. replica 2500X (15KV). It should be noted that a relatively thick coat of gold was applied to these replicas and they are examined at lower accelerating voltages.

- A. The Spurr's resin contained air bubbles, which had not had adequate time to settle out.
 - B. The Spurr's resin was cured at a temperature greater than 70°C. This is possible since the "flood lamp furnace" was not accurate but (usually) adequate.
 - C. The Spurr's resin was incorrectly measured and mixed, possibly changing the curing temperature.
7. Another possible source of error in preparing the replicas would be to apply too thick a coated layer of metal (Au or Pt). This could cover up (or fill in) fine detail such as very small cracks and surface features.
8. Use of this replicating technique allowed for the identification of very small surface features which lead to the tracing of specific characteristics; which would have otherwise been very difficult to find on the large fir-tree areas.

Figure 78, displays the replicating sequence: 0, 1,500, 15,000, 25,000, and 35,000 cycles of specimen F109-4 CR, N,: 47,302. This displays several important features about the replicating technique, as explained below:

1. By very careful observation of small topographical features

(see arrows) specific surface changes can be traced on all the replicas, even on the replicas which do not contain the feature being traced (crack only apparent in 35,000 cycles, and "growth" not apparent in 0 cycles).

2. If the replicas are not properly made, porous surfaces may develop. This is most extensively shown in the 15,000 cycle replica micrograph.

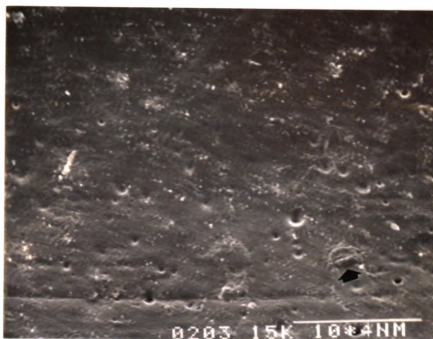
3. Even if surface pores are produced as a result of replicating error (in making the positive replica), small topographical features can usually still be seen and traced.

4. The development (or "growth") of certain surface features is evident with increasing fatigue life, the largest "growth" change of oxide polyps appears between 0 and 1,500 cycles.

5. Specimen cracks can be identified using this technique. A surface crack has become apparent between 25,000 and 35,000 cycles.

6. This series of replicas show the development of oxide polyps taking on a script-type morphology. The script morphology is seen in the lower central portion of the micrographs, just below the protruding sphere.

(a)



(b)

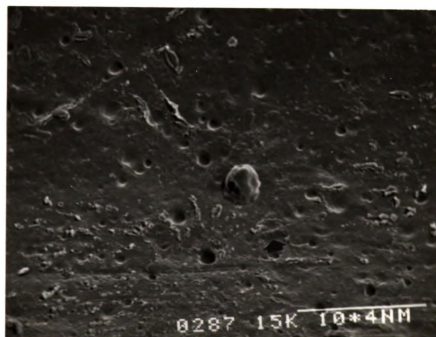
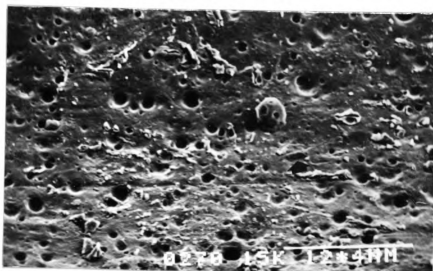


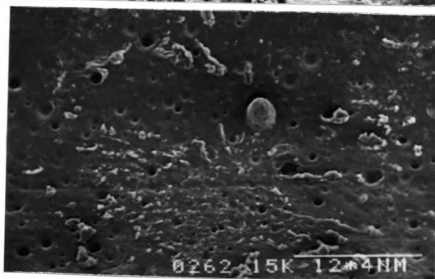
Figure 78. Replicating sequence of specimen F109-4 Cr:
a. 0 cycles, b. 1,500 cycles, c. 15,000 cycles,
d. 25,000 cycles and e. 35,000 cycles. RSEM 300X

Figure 78 (cont'd.).

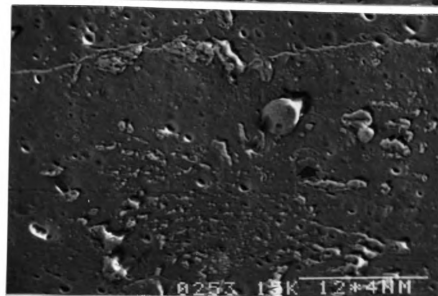
(c)



(d)



(e)



Supplementary reading:

C. H. Pameijer. "Replication Techniquesw with New Dental Impression Materials in Combination with Different Negative Impression Materials". Scanning Electron Microscopy, 2, 1979, pp. 571-574.

A. J. Spurr. "A Low-Viscosity Epoxy Resin Embedding Medium for Electron Microscopy". J. Ultra. Res., 26, 1969, pp. 31-34.

K. L. Klomparens, S. L. Fleger and G. R. Hooper. Procedures for Transmission and Scanning Electron Microscopy for Biological and Medical Science, A Laboratory Manual, 2nd ed. Center for Electron Optics, Michigan State University, 1986, pp. 112-114, & 127-132.

LIST OF REFERENCES

LIST OF REFERENCES

1. Sims, C. T. "High Temperature Alloys in High-Technology Systems", in High Temperature Alloys for Gas Turbines. Eds. D. Coutsouradis, et al, Applied Science Publishers, LTD, London, 1978, pp. 13-65.
2. Fulop, S. & McQueen, H. J. "Mechanisms of Deformation in the Hot Working of Ni-Base Superalloys" in Superalloys -- Processing, Proceedings of the Second International Conference. Metals and Ceramics Information Center, OH, 1972, pp. H-1 - H-21.
3. Tien, J. K. & Purushothaman, S. "The Metallurgy of High Temperature Alloys" in Properties of High Temperature Alloys, with Emphasis on Environmental Effects. Eds. Z. A. Foroulis & F. S. Pettit. The Electrochemical Society, Inc. NJ, 1976, pp. 3-41.
4. Giamei, A. F. et al. "Y/Y': The Key to Superalloy Behavior" in High Temperature Ordered Intermetallic Alloys, MRS Symposia Proceedings, Vol. 39, Eds. C. C. Koch et al. Materials Research Society, PA, 1985, pp. 293-308.
5. Decker, R. F & Sims, C. T. "The Metallurgy of Ni-Base Alloys" in The Superalloys. Eds. C. T. Sims & W. C. Hagel, John Wiley & Sons, NY, 1972, pp. 33-77.
6. Cole, G. S. & Cremisio, R. S. "Solidification and Structure Control in Superalloys" in The Superalloys. Eds. C. T. Sims & W. C. Hagel, John Wiley & Sons, NY, 1972, pp. 479-508.
7. Murata, Y et al. "Effect of Transition Elements on the Properties of MC Carbides in IN-100 Nickel-Based Superalloy". J. of Mat. Sci., 21, 1986, pp. 3653-3660.
8. Garosshen, T. J. & McCarthy, G. P. "Low Temperature Carbide Precipitation in Ni-Base Superalloy". Met. Trans. A, Vol. 16A, July 85, pp. 1213-1223.
9. Brooks, C. R. "Nickel-Base Alloys", in Heat Treatment Structure and Properties of Nonferrous Alloys. ASM, Metals Park, OH, 1982, pp. 139-228.

LIST OF REFERENCES (Continued)

10. Stoloff, N. S. "Fundamentals of Strengthening", in The Superalloys. Eds. C. T. Sims & W. C. Hagel, John Wiley & Sons, NY, 1972, pp. 79-111.
11. Huron, E. "High Temperature Monotonic and Cyclic Deformation in a D.S. Ni-Base Superalloy". NASA, CR-175101, NASA Lewis Research Center, OH, May 1986.
12. Gell, M. et al. "The Fatigue Strength of Nickel-Base Superalloys", in Achievement of High Fatigue Resistance in Metals and Alloys, pp. 113-153.
13. Kear, B. H. & Pope, D. P. "Role of Refractory Elements in Strengthening of and Precipitation hardened Nickel-Base Superalloys", in Refractory Alloying Elements in Superalloys. Eds. J. K. Tien & S. Reichman, ASM, Metals Park, OH, 1984, pp. 135-151.
14. Milligan, Jr., M. M. "Yielding and Deformation Behavior of the Single Crystal Nickel-Base Superalloy PWA 1480". NASA, CR-175100, NASA Lewis Research Center, OH, May 1986.
15. Scarlin, R. B. "Some Effects of Microstructure and Environment on Fatigue Crack Propagation", in Fatigue Mechanisms. Ed. J. T. Fong, ASTM STP 675, ASTM, PA, 1979. pp. 396-419.
16. Nathal, M. V. & Ebert, L. J. "Influence of Composition on the Microstructure and Mechanical Properties of a Ni-Base Superalloy Single Crystal", in Superalloys 1984. Eds. M. Gell et al, The Met. Society of AIME, PA, 1985, pp. 125-133.
17. Pettit, F. S. & Meier, G. H. "Oxidation and Hot Corrosion of Superalloys", in Superalloys 1984. Eds. M. Gell et al, The Met. Soc. of AIME, PA, 1985, pp. 651-687.
18. Whittle, D. P. "High Temperature Oxidation of Superalloys" in High Temperature Alloys for Gas Turbines. Eds. D. Coutouradis, et al, Applied Science Publishers, LTD, London, 1978, pp. 109-123.
19. Pettit, F. S. & Meier, G. H. "The Effects of Refractory Elements on the High Temperature Oxidation and Hot Corrosion of Superalloys" in Refractory Alloying Elements in Superalloys. Eds. J. K. Tien & S. Reichman, ASM, Metals Park, OH, 1984, pp. 165-174.

LIST OF REFERENCES (Continued)

20. Hart, A. B. & Cultler, A. J. B. eds. "Deposition of Corrosion in Gas Turbines". Appli. Sci., London, 1972, pg. 331.
21. Erickson, G. L. & Schwer, R. E. "Mar-M 247 Derivations - CM 247 LC DS Alloys, CMSX Single Crystal Alloys Properties & Performance", in Superalloys 1984. Eds. M. Gell et al, The Met. Soc. of AIME, PA, 1985, pp. 221-230.
22. Antolovich, S. D. & Jayaraman, N. "The Effect of Microstructure on the Fatigue Behavior of Ni-Base Superalloys" in Fatigue: Environment and Temperature Effects. Eds. J. J. Burke & V. Weiss, Plenum Press, NY, 1983, pp. 119-144.
23. Coffin, L. F. "Overview of Temperature and Environment Effects on Fatigue of Structural Metals" in Fatigue: Environment and Temperature Effects. Eds. J. J. Burke & V. Weiss, Plenum Press, NY, 1983, pp. 1-40.
25. Restall, J. E. "Surface Degradation and Protective Treatments" in The Development of Gas Turbine Materials. ed. G. W. Meetham, Applied Science Pub., LTD, London, 1981, pp. 256-290.
26. Coutts, Jr., W. H. "Refractory Elements Effects on Workability", in Refractory Alloying Elements in Superalloys. Eds. J. K. Tien & S. Reichman, ASM, Metals Park OH, 1984, pp. 69-76.
27. Ford, D. A. "Casting Technology" in The Development of Gas Turbine Materials. Ed. G. W. Meetham, Applied Science Pub. LTD., London, 1981, pp. 147-176.
28. McLean, M. & Schubert, F. "Mechanical Properties of Directionally Solidified Superalloys and Eutectics" in High Temperature Alloys for Gas Turbines. Eds. D. Couttsouradis, et al, Applied Science Pub., LTD, London, 1978, pp. 423-458.
29. Strangman, T. E., et al. "Development of Coated Single-Crystal Superalloy Systems for Gas Turbine Applications", in Superalloys 1984. Eds. M. Gell et al, The Met. Soc. of AIME, PA, 1985, pp. 795-804.
30. Sproles, Jr., E. S. & Duquette, D. J. "The Mechanism of Material Removal in Fretting". Wear, 49, 1978, pp. 339-352.

LIST OF REFERENCES (Continued)

31. Hurricks, P. L. "The Mechanism of Fretting - A Review". *Wear*, 15, 1970, pp. 389-409.
32. Murray, S. F. "Wear Resistant Coatings and Surface Treatments", in CRC Handbook of Lubrication (Theory and Practice of Tribology), Vol. II, Theory and Design. Ed. E. R. Booser, CRC Press, Inc., USA, 1984, pp. 623-644.
33. Barwell, F. T. "Report on Conference Papers on Wear". *Wear*, Vol 1 , 1957/58, pp. 431-434.
34. Forsyth, P. J. E. "Occurence of Fretting Fatigue Failures in Practice", in Fretting Fatigue. Ed. R. B. Waterhouse, Applied Science Pub. LTD, London, 1981, pp. 99-125.
35. Waterhouse, R. B. "Theories of Fretting Processes" in Fretting Fatigue. Ed. R. B. Waterhouse, Applied Science Pub. LTD, London, 1981, pp. 203-219.
36. Rabinowicz, E. "Wear Coefficients", in CRC Handbook of Lubrication (Theory and Practice of Tribology), Vol. II, Theory and Design. Ed. E. R. Booser, CRC Press, Inc. USA, 1984, pp. 201-208.
37. Hoepfner, D. W. "Environmental Effects in Fretting Fatigue", in Fretting Fatigue. Ed. R. B. Waterhouse, Applied Science Pub. LTD, London, 1981, pp. 143-158.
38. Barwell, F. T. "Metallic Wear", in CRC Handbook of Lubrication (Theory and Practice of Tribology), Vol. II, Theory and Design. Ed. E. R. Booser, CRC Press, Inc., USA, 1984, pp. 163-184.
39. Hondros, E. D. Tribology. Mills & Boon Limited, London, 1971.
40. Varin, J. D. "Microstructure and Properties of Super-alloys", in The Superalloys. Eds. C. T. Sims & W. C. Hagel, John Wiley & Sons, NY, 1972, pp. 231-257.
41. Hurricks, P. L. "The Occurrence of Spherical Particles in Fretting Wear". *Wear*, 27, 1974, pp. 319-328.
42. Scott, D. & Mills, G. H. "A Scanning Electron Microscopy Study of Fracture Phenomena Associated with Rolling Contact Surface Fatigue Failure". *Wear*, 16, 1970, pp. 234-237.

LIST OF REFERENCES (Continued)

43. Goss, G. L. & Hoepfner, D. W. "Characterization of Fretting Fatigue Damage by SEM Analysis". *Wear*, 24, 1973, pp. 77-95.
44. Scott, D. & Mills, G. H. Spherical Debris - Its Occurrence, Formation & Significance in Rolling Contact Fatigue". *Wear*, 24, 1973, pp. 235-242.
45. Stower, L. F., et al. *J. Appl. Phys.*, 43(5), 1972, pp. 2485-2487.
46. Bill, R. C. "Review of Factors that Influence Fretting Wear", in Materials Evaluation Under Fretting Conditions. Ed. S. R. Brown, ASTM STP 780, ASTM, PA, 1982, pp. 165-182.
47. Taylor, D. E. "Fretting Fatigue in High Temperature Oxidising Gases", in Fretting Fatigue. Ed. R. B. Waterhouse, Applied Science Pub. LTD, London, 1981, pp. 177-202.
48. Stott, F. H., Lin, D. S. & Wood, G. C. "The Structure and Mechanism of Formation of the "Glaze" Oxide Layers Produced on Ni-Base Alloys during Wear at High Temperatures". *Corrosion Science*, Vol. 13, 1973, pp. 449-469.
49. Engel, L. & Klingele, H. An Atlas of Metal Damage. Translated: S. Murray, Wolfe Pub. LTD, London, 1981.
50. Avner, S. H. Introduction to Physical Metallurgy. McGraw-Hill, Inc., USA, 1974.
51. Gell, M. & Leverant, G. R. "Fatigue of Nickel-Base Superalloys", in Ordered Alloys; Structural Applications and Physical Metallurgy. Eds. B. H. Kear et al, Claitors Publishing Division, LA, 1970, pp. 505-523.
52. Gaydo, J., Miner, R. V. & Gabb, T. P. "On the Fatigue Crack Propagation Behavior of Superalloys at Intermediate Temperatures", in Superalloys 1984. Eds. M. Gell et al, The Met. Soc. of AIME, PA, 1985, pp. 731-740.
53. Speidel, M. O. & Pineau, A. "Fatigue of High-Temperature Alloys for Gas Turbines", in High Temperature Alloys for Gas Turbines. Eds. D. Coutouradis, et al, Applied Science Publishers, LTD, London, 1978, pp. 469-512.

LIST OF REFERENCES

54. Fuchs, H. O. & Stephens, R. I. Metal Fatigue in Engineering. John Wiley & Sons, NY, 1980.
55. Waterhouse, R. B. "Avoidance of Fretting Fatigue Failures", in Fretting Fatigue. Ed. R. B. Waterhouse, Applied Science Pub. LTD, London, 1981, pp. 221-240.
56. Benson, D. K. "Surface Treatments for Fatigue Strengthening", in Achievement of High Fatigue Resistant Metals and Alloys. ASTM STP 467, ASTM, PA, 1969, pp. 188-208.
57. Endo, K. "Practical Observations of Initiation and Propagation of Fretting Fatigue Cracks", in Fretting Fatigue. Ed. R. B. Waterhouse, Applied Science Pub. LTD, London, 1981, pp. 127-141.
58. George, A. F. "A Comparative Study of Surface Replicas". Wear, 57, 1979, pp. 51-61.
59. Pameijer, C. H. "Replication Techniques with New Dental Impression Materials in Combination with Different Negative Impression Materials". Scanning Electron Microscopy, 2, 1979, pp. 571-574.
60. Gabriel, B. L. "Replicas", in SEM: A User's Manual for Materials Science. ASM, Metals Park, OH, 1985, pp. 137-147.
61. Marksteiner, J. P. "Investigation of Surface Strains in Fir Tree Turbine Blade Attachments". Thesis for M.S., Michigan State University, MI, 1985.
63. Hockin, J. "Investment Casting of Superalloys", in Superalloys -- Processing, Proceedings of the Second International Conference. Metals and Ceramics Information Center, OH, 1972, pp. C-1 - C-9.
64. Gemma, A. E., et al. "Thermomechanical Fatigue Crack Propagation in an Anisotropic (Directionally Solidified) Nickel-Base Superalloy", in Thermal Fatigue of Materials and Components. Eds. D. A. Spera & D. F. Mowbay, ASTM STP 612, ASTM, PA, 1976, pp. 199-213.
65. Denniston, W. E. "Comparison of Crowned and Uncrowned Blade Attachment Stress". Internal Report Garrett Turbine Engine Company, June, 1983.

MICHIGAN STATE UNIV. LIBRARIES



31293011041815